SAND2013-10618C

**2014-01-1272**

# Investigation of the Sources of Combustion Noise in HCCI Engines

**Jeremie Dernotte, John E. Dec, Chunsheng Ji**
Sandia National Laboratories

Copyright © 2014 SAE International

## Abstract

This paper presents an investigation toward a better understanding of the sources of HCCI combustion-generated noise and how it varies with engine load and speed. Two commonly used cylinder-pressure derived parameters were compared, the Combustion Noise Level (*CNL*) and the Ringing Intensity (*RI*), along with spectral analyses of the pressure traces. This study focuses explaining the differences between these two parameters and on investigating the sensitivity of the *CNL* to the ringing/knock phenomenon, to which the human ear is quite sensitive. Then, the effects of independently varying engine operating conditions such as fueling rate ($\Phi_m$ from 0.17 to 0.47), boost pressure (1.0 to 2.4 bar), and speed (600 to 2400 RPM) on both the *CNL* and the *RI* are studied.

Results show that the *CNL* is not significantly affected by the frequency components related to the ringing/knock phenomenon. On the contrary, *CNL* is found to be sensitive to increasing energy in the “low-frequency” range (from about 0.4 to 2.0 kHz) generated by the combustion-induced pressure rise. Parametric investigation shows that increasing the engine speed induces higher *CNL*, whereas it is not directly affected by the engine load. On the one hand, for a given boost pressure, the *CNL* was found to be nearly constant while increasing the fuelling rate. On the other hand, increasing the boost pressure (while holding the $\Phi_m$ constant) induces a significant increase in the *CNL* (by + 2.2 dB for a boost pressure variation from 1.0 to 2.0 bar). Results from this study emphasize the fact that the *RI* and the *CNL* are designed to provide two distinctly different but complementary measurements. *RI* appears to be a better suited criterion for the sake of combustion investigations to avoid knocking-combustion regimes, while *CNL* is valuable for determining the overall loudness of an engine.

## Introduction

Concerns about $CO_2$ reduction, urban air pollution and economic issues have led to increases interest in developing combustion systems for engines that are both highly fuel efficient and have low levels of harmful pollutant emissions. Homogeneous Charge Compression Ignition (HCCI) and HCCI-like combustion engines have been shown to be capable of providing high thermal efficiencies, and ultra-low $NO_x$ and particulate-matter emissions over a large range of operating conditions [1-3]. However, in spite of these advantages, several challenges remain to be addressed prior to its widespread implementation [3-6].

Among these challenges, the noise induced by the combustion process is a very important issue. In most cases, the HCCI combustion event is more rapid than that of conventional engines. HCCI combustion is generally characterized by a relatively high Pressure Rise Rate (*PRR*), which potentially generates two types of combustion noise. First, like any type of piston-engine combustion, a “base” noise is generated by the “normal” combustion process as a result of the uniform pressure rise associated with the combustion event. Compared to a Spark Ignition (SI) engine, the “base” noise of an HCCI engine might be expected to be greater, since the *PRR* tends to be higher. The noise could be somewhat closer to that of a conventional diesel-combustion process, which also features a relatively high *PRR* during the initial premixed phase of the combustion event.

The second combustion noise source for HCCI engines originates from the propensity of the combustion process to enter into the so-called “knocking” combustion regime. This potential for knock exists as operation is extended to higher loads, which can lead to higher *PRRs*, if steps are not taken to control them. As the *PRR* increases, it begins to generate acoustic pressure oscillations in the combustion chamber, called ringing in this article[1]. If the ringing becomes too intense, it eventually results in a distinctive, sharp and unpleasant sound, commonly known as knock.

Both, the base noise (induced by the “normal” combustion process) and the development of these acoustic pressure oscillations that can lead to knock, cause vibrations in the engine structure (block) that are subsequently radiated in the surrounding environment. Because of this, combustion-generated noise is a concern for HCCI-type engines. Furthermore, since noise radiated from the engine

---

[1] Terminology used in this article:
- Ringing is denoted as the acoustic pressure oscillations developing in the combustion chamber at the specific resonant frequencies of the cylinder.
- Knock is defined as the situation for which the ringing intensity becomes strong enough to cause the detrimental effects listed in the text.

compartment is among the important factors driving combustion-system design [7], there is a need to address the issue of combustion-generated noise from HCCI-type engines at a fundamental level.

In addition to its unpleasant sound, the occurrence of knock is associated with a substantial enhancement of the heat-transfer losses, believed to be due to a breakdown of the thermal boundary layer by the velocity oscillations associated with the resonating pressure waves [8]. Under certain conditions, generally due to either the load increasing or the combustion being phased too close to the Top Dead Center (TDC), the additional heat-transfer losses induced by the knock phenomenon can cause a drop of the thermal efficiency [9]. Finally, in extreme cases, it is considered that intense HCCI knock could result in engine physical damage over time (somewhat similar to the effect of knock in SI engines).

Knock in HCCI-like engines differs from the knocking phenomenon occurring in SI engines. For the latter, knock is a consequence of end-gas autoignition before the combustion by flame propagation complete. Because the mixture is stoichiometric, the autoignited end-gas combusts very rapidly, causing a localized rapid pressure rise that excites acoustic resonance frequencies in the cylinder. In HCCI engines, the mixture is dilute, either by being very lean or with high Exhaust Gas Recirculation (EGR) levels. Moreover, the entire combustion chamber contains significant thermal stratification due to heat transfer/convection effects [10]. This results in a slower and more progressive autoignition than in the end gas of SI engines.

The process that leads to HCCI knock is also more progressive than that of SI engines [11, 12]. As the fueling rate is increased and the mixture becomes less dilute, or the combustion phasing is less retarded, the combustion rate becomes more rapid, as indicated by a higher *PRR*. Low amplitudes ripples appear on the pressure trace, and a spectral analysis of the pressure trace (*i.e.* Fast-Fourier-Transform of the pressure signal) shows a corresponding low power content at the frequency of these ripples. If the *PRR* is not too rapid, this can occur without the aforementioned detrimental consequences of the knock phenomenon. As the *PRR* is progressively increased due to further increases in the fueling or decreases in combustion-timing retard, the magnitude of these ripples increases as does the corresponding spectral power content at these frequencies. Eventually, the magnitude of the acoustic pressure oscillations reaches the point that the engine is said to be knocking, as will be discussed in detail in the later sections of this article.

The exact mechanism whereby this more rapid combustion excites acoustic resonances is not completely understood. It is likely that initial oscillations are triggered by a relatively high combustion rate of some localized zones at multiple locations within the charge [3, 13-15], that interact with each other in a way that excites the acoustic modes of the cylinder. The characteristic frequencies (*i.e.* resonance modes) excited can be well estimated using the solution of the wave equation for a right circular cylinder (Draper's equation [2]) [11, 12, 15-17]. The majority of the pressure oscillations' acoustic power and the corresponding sources of the noise from the knock phenomenon are mainly contained in the first circumferential resonant mode (centered at ~ 3 to 6 kHz, depending on the in-cylinder temperature and cylinder bore diameter) [12, 16].

Several in-cylinder pressure-derived metrics (noise related) are commonly employed to characterize the combustion process in HCCI-like engines. They are also valuable for adjusting and optimizing the HCCI-engine control parameters to keep it operating well. These metrics are: the Peak Pressure Rise Rate (*PPRR*), the Ringing Intensity (*RI*) and the Combustion Noise Level (*CNL*) [3], as introduced in the following.

1. The *PPRR* represents one of the main cylinder pressure characteristics. It is the most basic of these metrics and is simply the maximum rate of pressure rise during the combustion event. Early HCCI works [3] used *PPRR* almost exclusively to set a limiting criterion for the harshness of HCCI combustion. However, it was found that a single value of the *PPRR* did not provide consistent results over changes in many engine parameters such as speed and boost pressure. It has now largely been superseded by the other techniques.
2. The *RI*, as proposed by Eng [11], is a quantity that is correlated with the acoustic energy of the resonating pressure wave (expressed in $\mathrm{MW/m^2}$) in order to quantify the propensity of the combustion to produce acoustic oscillations. It is a convenient and well-accepted metric to forecast excessive oscillations (*i.e.* knock). By setting a criterion for the *RI*, the onset of knock can be fairly well predicted over a wide range of operating conditions [3].
3. Finally, the *CNL* is a commonly used metric that aims at estimating the combustion-induced noise. The cylinder pressure is converted to the frequency domain where it is filtered by a transfer function to predict the combustion noise transmitted through the engine structure and to account for how this transmitted noise is perceived by the human ear [18].

Other metrics have been developed to characterize the ringing/knock phenomenon, mainly based on the analysis of the pressure fluctuation amplitudes of the acoustic oscillations [8, 11, 12, 14, 19, 20]. In this study, the Knock Index (*KI*) will be introduced as a measure of the power in the first acoustic mode. It will be applied for a specific dataset.

Several studies have investigated how the first three metrics (*PPRR*, *RI*, *CNL*) compare over a wide range of operating conditions (speed/load) and Low Temperature Combustion (LTC) modes [2, 18, 21, 22]. They all generally agree that for small changes about a given engine operating point, variations in *CNL* correlate well with changes in either the *PPRR* or the *RI* (*e.g. CNL* increases when either *PPRR* or *RI* is increased). However, there are some significant discrepancies with larger changes the operating conditions, or when combustion modes or engine platforms are changed. Poor correlations between the *CNL* and the *RI*, and a somewhat better correlation of *CNL* with the *PPRR,* are reported. For instance, the *CNL* substantially increases with engine speed and more moderately with boost pressure for a given *PPRR* or *RI*. It was therefore concluded in the aforementioned studies, that neither

---

[2] Draper's equation is presented in the next section: Equation 4.

[3] Detailed descriptions of these metrics (particularly the *RI* and the *CNL*) is provided in the next section.

the *PPRR* nor the *RI* well represent the noise emitted by the combustion process.

Accordingly, it is of interest to better understand the sources of the combustion-generated noise and how the various metrics respond to this noise over a wide range of operating conditions. This is the main objective of the present study which is targeted at providing a fundamental understanding in order to correctly interpret *CNL* and *RI* results derived from cylinder-pressure measurements in HCCI-like engines. This is particularly needed for the development of noise control/reduction strategies. Toward these goals, combustion characterization metrics (*PPRR*, *CNL* and *RI*) are compared along with spectral analyses of the pressure traces. This study has been conducted on the analysis of in-cylinder pressure traces recorded from a single cylinder HCCI research engine (~ 1 liter displacement) over a wide range of practical operating conditions.

In the following section the experimental facility and data-acquisition techniques are described, and detailed descriptions of the various cylinder-pressure analysis techniques are provided. Then, the results of the current study are presented in two parts. In the first part, the study particularly focuses on investigating the sensitivity of the *CNL* to the ringing/knock phenomenon, to which the human ear is quite sensitive. To do so, raw and low-pass filtered pressure traces that truncate the knock frequency components are compared using a dataset for which the knock-onset point is well defined. Further analysis leads to the identification of the frequency range responsible for the overall loudness of the combustion process. In the second part of the results, the main engine operating parameters (*i.e.* load and speed) are varied over a wide range ($IMEP_g$ from 2.5 to 16.0 bar and engine speed from 600 to 2400 RPM). This is particularly relevant in the context of the development of high-load, high-speed HCCI engines. The individual effects of the equivalence ratio and the boost pressure on the *CNL* are also investigated and interpreted. Finally, in the last section, the results are summarized, conclusions drawn and areas where further research is needed are identified.

## Experimental Setup & Data Acquisition

### *Engine Facility*

The HCCI research engine used for this study was derived from a Cummins B-series six-cylinder diesel engine, which is a typical medium-duty diesel engine with a displacement of 0.98 liters/cylinder. Figure 1-a shows a schematic of the engine, which has been converted for single-cylinder operation by deactivating cylinders 1-5. The engine specifications and main operating conditions are listed in Table 1. Additional information on the facility may be found in Ref. [23].

Data for the present study have been obtained using two different pistons, giving geometric Compression Ratios (*CR*) of 14:1 and 16:1 as shown in Figure 1-b. The *CR* = 14:1 piston was used in several previous studies, like in ref. [9], and some of the data acquired in the aforementioned reference have been re-analyzed in terms of *CNL*. Additionally, new data have been acquired with a recently installed *CR* = 16:1 piston. The *CR* = 14:1 custom piston provides an open combustion chamber with a large squish clearance and a quasi-hemispherical bowl (Figure 1-b). Comparison tests showed minimal differences in performance and emissions compared to the *CR* = 14:1 broad shallower-bowl piston as used in earlier studies, *e.g.* [24-26]. The *CR* = 16:1 custom piston is also characterized by a broad shallow bowl as shown by Figure 1-b. Both of these pistons provide a small topland ring crevice, amounting to less than 0.9% of the TDC volume. Although one to one *CR* comparison is not included in this paper, differences in terms of *CNL* were found to be small (*e.g.* less than 1 dB for a typical intake-boosted operating point with $P_{in}$ = 2.4 bar, $T_{in}$ = 30˚C, early DI fueling and over a large range of fueling rates).

Table 1. Engine specifications and operating conditions

| | |
|---|---|
| Displaced (single cylinder) | 0.981 liters |
| Bore | 102 mm |
| Stroke | 120 mm |
| Connecting rod length | 192 mm |
| Geometric compression ratio | 14:1 & 16:1 |
| Number of valves | 4 |
| IVO | 0°CA * |
| IVC | 202°CA * |
| EVO | 482°CA * |
| EVC | 8°CA * |
| Swirl ratio | 0.9 |
| Fueling system | Fully premixed and GDI |
| GDI injector<br>Included angle<br>Hole size<br>Injection pressure | Bosch, 8-hole<br>70˚<br>Stepped-hole, min. dia. = 0.125 mm<br>120 bar |
| Engine speed | 600 to 2400 RPM |
| Centerline intake temperature | 30 to 181˚C |
| Intake pressure (abs.) | 1.0 to 2.4 bar |
| Coolant temperature | ~ 100˚C |

** 0°CA is taken to be TDC intake. The valve-event timings correspond to 0.1 mm lift.*

As shown in Figure 1-a, the EGR loop is equipped with a cooler (a gas-to-water heat exchanger), and the EGR is introduced well upstream of the intake plenum. The EGR travels with the intake air through a series of bends before reaching the intake plenum, to insure that the intake charge is well mixed. With this configuration, the exhaust pressure must be greater than the intake pressure for EGR to flow into the intake. The required back pressure was achieved by throttling the exhaust flow using the valve shown in Figure 1-a. Intake air was supplied by an air compressor and precisely metered by a sonic nozzle as shown in Figure 1-a. Intake pressures varied from 1.0 bar (simulating naturally aspirated conditions) to 2.4 bar for the current study. All pressures given are absolute. For operation without EGR, the air flow was adjusted to achieve the desired intake pressure, as measured by a pressure transducer on the intake runner. The air flow was reduced from the amount required to achieve the desired intake pressure with air alone, and the valve on the EGR line was opened. The exhaust back-pressure throttle valve was then adjusted to produce enough EGR flow to reach the desired intake pressure. This typically resulted in the exhaust pressure being about 2 kPa greater than the intake pressure. For consistency, the back pressure was maintained at 2 kPa above the intake pressure, even when EGR was not used. The EGR fraction was varied by adjusting the amount of supplied air, and then adjusting the exhaust throttle to maintain the desired intake pressure.

The premixed fueling system, shown at the top of the schematic in Figure 1-a consists of a GDI injector mounted in an electrically heated fuel vaporizing chamber and appropriate plumbing to ensure thorough premixing with the air and EGR upstream of the intake plenum. The DI fueling is accomplished using a second GDI injector mounted centrally in the cylinder head. A positive displacement fuel flow meter was used to determine the amount of fuel supplied.

Depending upon the dataset presented in the results section, two different gasolines were used, but not compared. They include a research-grade regular gasoline supplied by Chevron-Phillips Chemical Co. and a high-octane certification gasoline from Haltermann Solutions. Neither gasoline contained ethanol. The fuel specifications are listed in Table 2.

Similar to some of our other recent works [27, 28], this work uses an equivalence ratio based on total charge mass, rather than air alone. This equivalence ratio, referred to as the charge-mass equivalence ratio ($\phi_m$), is defined by Equation 1, where *F/C* is the mass ratio of fuel and total inducted charge gas (*i.e.* fresh air and EGR), and $(F/A)_{stoich}$ is the mass ratio of stoichiometric fuel/air mixture for complete combustion. This provides a convenient and consistent way to compare data with the same supplied energy content per unit charge mass (*i.e.*, the same dilution level) for operating conditions with different fuels and different EGR levels. Note that $\phi_m$ is the same as conventional air-based $\phi$ when no EGR is used. It should also be noted that the air-based $\phi$ is < 1 for all conditions presented, so combustion is never oxygen limited.

$$\emptyset_m = {}^{(F/C)}\!\Big/_{(F/A)_{stoich}} \tag{1}$$

Prior to starting the experiments, the engine was fully preheated to 100°C by means of electrical heaters on the "cooling" water and lubricating-oil circulation systems. In addition, the intake tank and plumbing were preheated to a minimum temperature of 60°C to avoid condensation of the fuel in the case of the premixed fueling system. The minimum intake temperature in the case of the DI injection was 30°C. An auxiliary heater mounted close to the engine provided precise control of the centerline intake temperature to maintain the desired combustion phasing. Intake temperatures ranged from 30 - 181°C in this present study. All data were taken at an engine speed of 1200 rpm unless otherwise specified, particularly for the case for which the engine speed effect on the *CNL* was investigated.

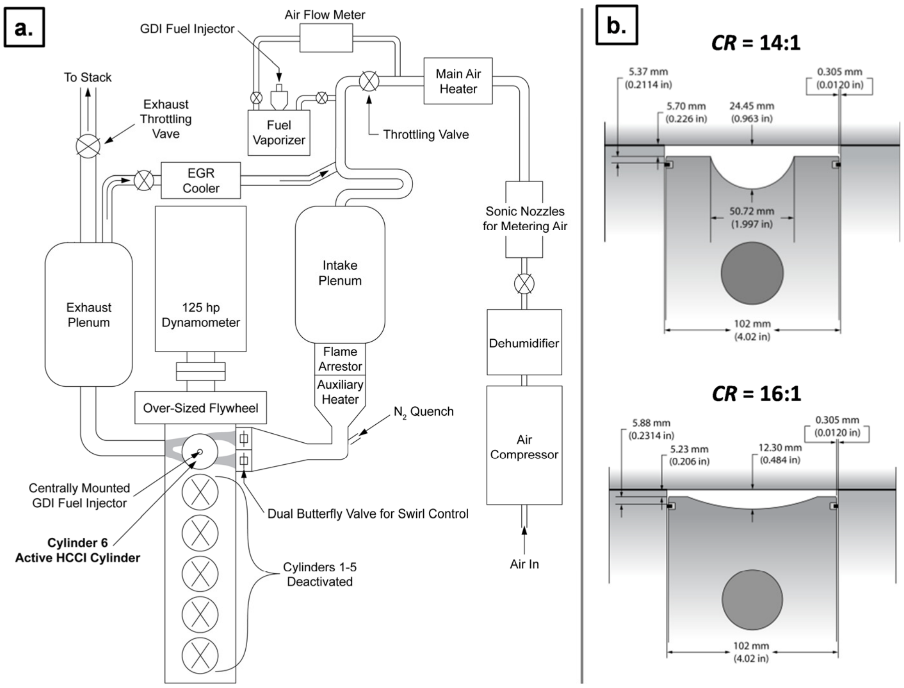

Figure 1. Schematic of the HCCI engine facility (a.) and combustion chamber geometries of the *CR* = 14:1 and 16:1 at TDC (b.)

Table 2. Fuel properties

| | Chevron-Phillips Research-Grade Gasoline * | Haltermann Solutions Certificate Gasoline |
|---|---|---|
| **Antiknock Index (R+M)/2** | 86.9 | 92.7 |
| **RON** | 91.0 | 96.6 |
| **MON** | 82.7 | 88.7 |
| **Specific gravity** | 0.746 | 0.743 |
| **Carbon [wt%]** | 86.37 | 86.49 |
| **Hydrogen [wt%]** | 13.55 | 13.34 |
| **Oxygen [wt%]** | 0.08 | None detected |
| **A/F Stoichiometric** | 14.60 | 14.56 |
| **Lower Heating Value, gas-phase [MJ/kg]** | 43.10 | 42.97 |
| **LHV for stoichiometric charge [MJ/kg]** | 2.763 | 2.762 |
| **Hydrocarbon type [vol%]** | | |
| Aromatics | 24.5 | 34.3 |
| Olefins | 5.1 | 0.12 |
| Saturates | 70.1 | 64.0 |
| **Distillation [˚C]** | | |
| 5% | 56.9 | 43.3 |
| 10% | 63.4 | 52.8 |
| 30% | 78.9 | 80.6 |
| 50% | 96.1 | 106.1 |
| 70% | 114.1 | 117.8 |
| 90% | 147.3 | 159.4 |
| 95% | 164.9 | 172.8 |

** Based on analysis provided by Paragon Labs, Inc.*

## *Data Acquisition*

Cylinder pressure measurements were made with a transducer (AVL QC33C) mounted in the cylinder head approximately 42 mm off center. The pressure transducer signals were digitized and recorded at ¼° CA increments for one hundred consecutive cycles. The cylinder-pressure transducer was pegged to the intake pressure near Bottom Dead Center (BDC) where the cylinder pressure reading was virtually constant for several degrees. Centerline intake temperatures were monitored using thermocouples mounted in the two intake runners close to the cylinder head. For all data presented, 0° Crank Angle (CA) is defined as TDC intake (so TDC compression is at 360°CA). This eliminates the need to use negative crank angles or combined before-TDC, after-TDC notation.

The crank angle of the 50% burn point (*CA50*) was used to monitor the combustion phasing. *CA50* was determined from the cumulative Apparent Heat-Release Rate (AHRR), computed from the low-pass filtered cylinder-pressure data [23]. Computations were performed for each individual cycle, disregarding heat transfer and assuming a constant ratio of specific heats [29]. The average of 100 consecutive individual cycle *CA50* values were then used to monitor *CA50* during engine operation and for the values reported. The reported Pressure Rise Rates (*PRR)* and Ringing Intensities (*RI*) are computed from the same low-pass-filtered pressure data. For each cycle, the Peak *PRR* (*PPRR*) was analyzed separately with a linear fit over a moving ±0.5°CA window (5 points). Similar to *CA50*, these individual-cycle values were then averaged over the 100-cycle data set. Examples of the effect of the filtering algorithm will be shown later in relation to Figure 7 and Figure 18. The high-frequency-reject filter was set so that frequencies below 2.5 kHz were unaffected, while frequencies from 2.5 to 3.9 kHz were progressively attenuated using a Gaussian roll-off function. As evident in Figure 7 (and also demonstrated in [23]), this smoothly truncates the frequency power spectrum at the near-zero region between the lower frequencies due to combustion and the higher frequencies due to knock.

## *Data Analysis Methods*

### Ringing Intensity (*RI*)

The operating range of HCCI engines is often limited at high loads by the occurrence of the knock phenomenon. It originates from conditions producing a relatively high HRR which triggers pressure oscillations at specific resonant acoustic modes within the combustion chamber. If left uncontrolled, the HRR rate could reach unacceptable levels and generates a sharp and unpleasant distinctive sound, commonly referred as engine knock. The knock effect could cause an substantial increase in the heat transfer and then, under certain conditions (generally either as load increases or as the combustion is getting more advanced [4]), a drop of the thermal efficiency [8, 9]. Finally, it is considered that intense HCCI knock could results in engine physical damage over time.

On the other hand, for a given engine load, in order to maximize the thermal efficiency, it is desirable to advance the combustion phasing (when *CA50* occurs later than ~ 366˚CA) to take advantage of higher expansion ratio [9]. However, advancing *CA50* can increase the combustion rate [5]. As a result, it is appealing to operate the engine as close as possible (considering a safety margin) to the knock onset limit.

It has now been well established [1, 11, 30-33] that the acceptable ringing limit for HCCI engines is not correctly captured by setting a fixed criterion on the maximum allowable *PRR* ($dP/d\theta$, where $\theta$ is a variable representing °CA) under different engine speeds and boost pressures. In these aforementioned references' experimental observations, it was noticed that with higher boost levels the combustion chamber could withstand higher PRRs without producing an undue increase in the characteristic audible knocking sound. This is thought to be the result of the increased dampening effect of the pressure waves by the higher in-cylinder density [11, 33]. Moreover, during HCCI combustion, it is likely that weak pressure oscillations (*i.e.* "light" ringing) occur even without any of the detrimental consequences of the knock phenomenon (*i.e.* characteristic knocking sound, lost in thermal efficiency, engine physical damages) [11, 12]. Consequently, the pathway leading to knock is progressive and a criterion needs to be

---

[4] An example will be provided in the results section in relation to Figure 4.

[5] This aspect will be further discussed in the results section.

defined to set a boundary between non-knocking and knocking combustion regimes.

In this work, the correlation for ringing intensity (Equation 2) developed by Eng [11] is introduced to indicate the propensity for engine knock. The *RI*, expressed in MW/m$^2$, is a measure that correlates with the acoustic energy of the resonating pressure wave.

$$RI \approx \frac{1}{2\gamma} \cdot \frac{\left(\beta \cdot \left(\frac{dP}{dt}\right)_{\max}\right)^2}{P_{\max}} \cdot \sqrt{\gamma . R . T_{\max}} \tag{2}$$

This correlation includes the in-cylinder main conditions, namely $(dP/dt)_{max}$, $P_{max}$, and $T_{max}$ which are the peak values of the *PRR* (in real time: kPa/ms), pressure, and mass-averaged temperature, respectively, $\gamma$ is the ratio of specific heats $(c_p/c_v)$, and *R* is the gas constant. The *PPRR* [6] was obtained from the low-pass-filtered pressure traces as previously mentioned, converted to real-time by using the average crankshaft speed. The use of a time-based *PPRR* as opposed to the crank angle based one is intended to eliminate the engine speed dependence, according to Eng [11]. For this study, the computation of the *RI* using Equation 2 was performed based on the *PPRR* averaged over 100 cycles together with the peak mass-averaged temperature and pressure from the ensemble-averaged pressure trace.

The term $\beta$ is an empirically determined scaling coefficient. It relates the *PPRR*, which is considered to be the main input force that drives the combustion chamber into acoustic resonance, to the largest peak-to-peak amplitude of the induced pressure oscillations: $\Delta P = \beta . (dP/dt)_{max}$. According to Eng [11], the amplitude of pressure oscillations is in the order of 5% of the *PPRR*. However, the range of operating conditions over which this assumption is valid is not clearly specified. For instance, as reported by Maria *et al.* [32], it is expected that $\beta$ should significantly decreases with peak pressure and therefore with the boost level. Indeed, from our experimental observation, for any given *PPRR*, the amplitude of the pressure oscillations decreases as the cylinder pressure increases. However, it is unclear whether this indicates a need to adjust $\beta$ with boost, or if the increase in $P_{max}$ with boost in the denominator of Equation 2 is sufficient to compensate. Based on our experience with this engine at all boost levels tested [1] (*i.e.* $P_{in}$ = 1.0 to 3.2 bar) and mainly at 1200 RPM, using $\beta$ = 0.05 ms as a constant (like Eng), a *RI* criterion of 5 MW/m$^2$ was found to correlate well with the onset of an audible knocking sound and the appearance of obvious ripples on the pressure trace. For comparison, this *RI* threshold of 5 MW/m$^2$ selected for operation without knock corresponds to about 8 bar/°CA at 1200 RPM, naturally aspirated. A second critical assumption concerns the use of the peak values for the cylinder pressure and the mass-average temperature. This is originally based on experimental observation that the pressure oscillations begin to appear just after the peak cylinder pressure. This assumption is in accordance with the results of Dahl *et al.* [15] using high speed imaging. They found that the first mode acoustic oscillations almost always appear to develop from rapidly combusting regions late in the cycle.

## Combustion Noise Level (*CNL*)

In this study, the Combustion Noise Level (*CNL*) was estimated through the analysis of the in-cylinder pressure according to the algorithm described by Shahlari *et al.* [18], who also showed that the output of this algorithm matches well with the AVL combustion noise meter. This method consists of converting the complete cylinder pressure trace (whole cycle) into the frequency domain by applying a Fast Fourier Transform (FFT) to obtain the Power Spectral Density (PSD). Two filters are applied to the PSD, one to simulate the attenuation by the engine structure and the other to account to the response of the human ear (known as the A-filter). Figure 2 illustrates the two filters along with a typical PSD. Notice that the two filters are plotted using two different y-axis scales shown on the right hand side of the figure. Note from these scales that the effect of the A-filter is much smaller than that of the engine structure filter. Therefore, the PSD of the in-cylinder pressure trace is mainly attenuated by the engine-structure, and in the following plots, only the structure-attenuation filter will be presented. To compute the *CNL*, the resulting attenuated signal is then integrated over the whole frequency range to obtain the Sound Pressure (*SP*). It is finally converted to decibels by comparing the *SP* to the human hearing threshold (20 μPa). The *CNL* calculation is performed for each individual cycle and then is ensemble-averaged.

The noise can also be expressed in terms of power emitted per unit of surface (linear scale), as given by the Intensity of Sound ($I_{sound}$):

$$I_{sound} = \left({}^{SP}/_{K}\right)^2 \tag{3}$$

where $K = \sqrt{\rho . c}$, with $\rho$ and $c$ are the density of the medium (room air density) and the velocity of sound in the medium ($c = \sqrt{\gamma . r . T_{room}}$).

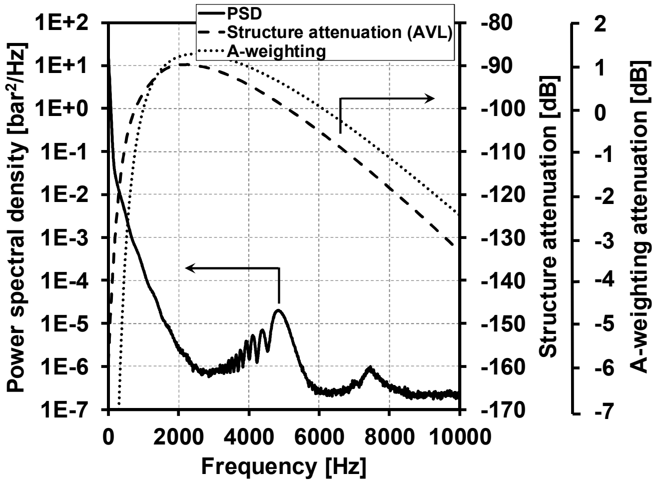

Figure 2. Example of a frequency spectrum of a cylinder pressure trace with the "generic" engine structure attenuation curve and A-weighting filter from Ref. [18], *RI* ≈ 5 MW/m$^2$ (onset of knock).

As pointed out by Torregrosa *et al.* [34], this approach to estimate the *CNL*, assumes a "generic" engine structure attenuation filter that behaves as a linear system regardless of

---

[6] *PPRR* is used as the main acronym in this article, standing for Peak Pressure-Rise Rate. The time-based *PPRR* is equivalent to $(dP/dt)_{max}$ while the crank angle-based *PPRR* is equivalent to $(dP/d\theta)_{max}$.

the engine operating conditions. Therefore, it does not consider among other factors, the complex patterns of acoustic energy propagation through the engine structure and its non-linearity with time (acceleration of the block). Despite these assumptions, the use of the methodology is considered consistent in the sake of the combustion study.

The *CNL* is derived by integrating the PSD of the pressure trace. The highest frequency (*i.e.* the Nyquist frequency) contained in the PSD depends on the shaft-encoder resolution and the engine speed. If the sampling rate is too low (not fine enough encoder resolution or engine speed is too low), the aliasing phenomenon might bias the resulting PSD and then the *CNL*. It was found that with the current encoder resolution (¼°CA increments) for the engine speed range investigated in this study (600 to 2400 RPM), the aliasing phenomenon does not significantly bias the results. The maximum induced error was about + 0.4 dB (at 600 RPM).

## Knock Index (*KI*) and Vibration Modes

As part of this work, the Knock Index (*KI*) is introduced as an additional means of characterizing the intensity of the ringing phenomenon. This metric is used in the first section of the results to support the selection of $RI \approx 5$ MW/m$^2$ as a well-suited parameter to detect the onset of knock. The *KI* is defined as the integral of the PSD over first acoustic resonant mode for an appropriate frequency range as illustrated on Figure 3. A frequency range of 3.0 to 6.2 kHz was used as shown in the figure, but the exact values for the limits of integration are not critical. This mode has been chosen because it contains the majority of the acoustic wave energy [11, 12, 15, 16, 22]. This metric correlates directly with the information contained in the largest pressure oscillations seen on the pressure trace while ringing (acoustic oscillations) is present.

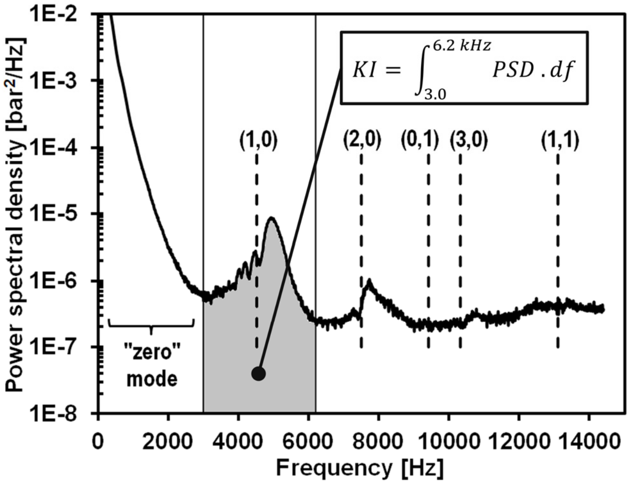

Figure 3. Definition of the Knock Index (*KI*) used in this study. The dash lines represent the frequency modes (*m,n*) estimated according to Equation 4. $RI \approx 5$ MW/m$^2$ (onset of knock)

From the plot in Figure 3, it can also been seen the estimated first five vibration modes (*m,n*) represented by the straight vertical dashed lines, calculated from solution of the wave equation for a simplified circular cylinder (Equation 4 and Table 3) [17]. In Equation 4, $f_{m,n}$ is the resonant frequency for the *m* (circumferential) and *n* (radial) pressure node, $\alpha_{m,n}$ is the wave number given in Table 3, $\sqrt{\gamma\,.r\,.T_{cyl}}$ is the speed of sound approximated in this study at the mass-average peak temperature and *B* is the cylinder bore diameter. As seen in Figure 3, only the first (1,0) and second (2,0) circumferential modes could be clearly identified from the derived PSD, while the third circumferential mode (3,0) seems to hardly appear. The radial modes are not present on this PSD. Perhaps this is due to the location of the pressure sensor (42 mm off center) which might correlate with the corresponding acoustic radial nodes (compare with schematic in Table 3), or perhaps the radial modes are just very weak or non-existent.

In addition to these acoustically resonant modes, the contribution to the PSD of the "normal" combustion process will be defined as the "zero" mode in this study as indicated on this figure (0 to ~ 3000 Hz range). This mode is by nature, not resonant. It does not include any significant contribution due to acoustic pressure oscillations. Instead, it is induced by the uniform pressure rise due to the pressure rise.

$$f_{m,n} = \alpha_{m,n}\,.\frac{\sqrt{\gamma\,.r\,.T_{cyl}}}{\pi\,.B} \tag{4}$$

Table 3. Vibration modes for the right circular cylinder [17]

| | 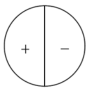 | 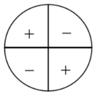 | 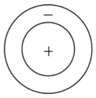 | 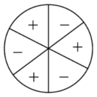 | 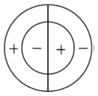 |
|---|---|---|---|---|---|
| **(*m,n*)** | (1,0) | (2,0) | (0,1) | (3,0) | (1,1) |
| **$\alpha_{m,n}$** | 1.841 | 3.054 | 3.832 | 4.201 | 5.332 |

Finally, it must be mentioned that the information contained in the vibration modes (including the *KI*), needs to interpreted with caution and thus qualitatively. Several factors might contribute to uncertainty and inconsistency in obtaining quantitative information from analysis of these modes. First, it has been demonstrated that monitoring these acoustic oscillations is sensitive to the location of the pressure sensor relative to the wave propagation direction [15, 16]. Sufficient ensemble-averaging should mitigate this phenomenon, due to the assumed randomness of the zone locations generating the acoustic oscillations. However, results might be inconsistent, depending on whether or not there is a preferred direction for the resonant wave propagation at the condition of interest. For example, for the first circumferential mode (1,0), the pressure transducer will see much larger oscillations if it is in-line with direction of the pressure oscillation rather than perpendicular to it. For this reason, it is also expected that the acoustic modes' contribution to the *CNL*, if any, could vary depending on the direction of the wave and the transducer location. Second, there is uncertainty due to the phasing at which these oscillations are developing relative to the combustion event. This could affect the gas temperature, and therefore the resonant frequency of the oscillations (Equation 3) [22]. Also, the timing of the oscillations relative to the expansion process, could affect the amplitude of these pressure waves and the number of periods for the waves to travel back and forth in the cylinder. Third, in regard to the *KI* calculation, the first mode power content might overlap the "zero" mode under some conditions affecting the accuracy of the computed *KI*.

# Results & Discussion

## *Comparison between the Combustion Noise Level and the Ringing Intensity*

The main objectives of this section are to compare the *CNL* with the *RI*, and to investigate whether the *CNL* is sensitive to the onset of knock. First, the *RI* threshold of 5 MW/m$^2$ for the onset of HCCI knock is compared with other common means to detect the onset of knock for selected operating conditions. Second both metrics (*CNL* and *RI*) are compared.

For a given boost pressure, the *RI* can be varied by adjusting one or more operating parameters, such as the intake temperature, the EGR rate or/and the fueling rate [9]. In the following case, to investigate the relationship between the *RI* and the *CNL*, previously published datasets [9] dealing with the effects of fueling rate on the thermal efficiency, have been analyzed. They consist of two $\Phi_m$ sweeps shown in Figure 4, first without and then with EGR addition to control the *RI*. The intake pressure and temperature were held constant ($P_{in}$ = 2.0 bar, $T_{in}$ = 30˚C). Some selected low-pass filtered and ensemble averaged cylinder-pressure traces and heat release rates are displayed in Figure 5, corresponding to the four highlighted operating points, labeled from 1 to 4 (on the *RI* curves) in Figure 4-a. They show the effects on the combustion process of increasing the *RI* and $\Phi_m$ (operating points #1, 2 & 4), and holding the *RI* constant as $\Phi_m$ increases (operating point #2 & 3). These datasets have been selected for the current study because they represent a particular case for which the knock onset is not only characterized by a *RI* of ~ 5 MW/m$^2$, but also by a drop in the thermal efficiency due to higher heat transfer caused by the knock phenomenon, as it will be described in the following. Hence, it includes a measurable parameter confirming the presence of knock other than the subjective onset in audible knocking characteristic noise for *RI* > ~ 5 MW/m$^2$. Moreover, as stated previously, beyond than just looking at the appearance of significant ripples on the pressure trace, the knocking frequency components, particularly the first mode (which contains most of the knocking power), are analyzed by the mean of the *KI* (Figure 3).

The first sweep, shown by the filled-symbol data points in Figure 4, represents the case for which the fueling rate, quantified by $\Phi_m$, was increased from 0.304 to 0.332. Because no EGR was used and the intake temperature was held constant ($T_{in}$ = 30˚C), the *CA50* advanced from 368.9 to 365.2˚CA with this fueling increase. As can be seen on Figure 4-a, this increase in the fueling results in an increase in the *RI* from 1.9 to 9.9 MW/m$^2$. Referring to the *RI* equation (Equation 2), despite an increase in the peak pressure (from 100 to 126 bar, Figure 5), this increase in the *RI* is a consequence of a rapid increase in the *PPRR* from 7.0 to 17.6 bar/˚CA (as can be seen in Figure 5) along with a moderated increase in the mass-averaged peak temperature (1494 to 1673 K). These effects are caused by combination of the increased pressure rise resulting from the higher $\Phi_m$ and a more advanced *CA50*. The latter occurs because the higher-$\Phi_m$ mixture is more reactive at this boost level, and because the higher $\Phi_m$ increases the wall temperatures and the residual-gas temperatures increasing the initial charge temperature (see ref. [9] for further explanations).

For the second sweep, showed by the empty symbols, *CA50* was retarded (from 367.8 to 373.8˚CA) by adding progressively more EGR as $\Phi_m$ was increased from 0.321 (no EGR) to 0.412. Retarding *CA50* in this manner, controlled the *PPRR* and peak pressure to hold the *RI* constant at ~ 5 MW/m$^2$ (refer to Equation 3). This strategy is commonly employed to reach higher loads, without excessive ringing [1]. Eventually, however, *CA50* becomes so retarded that combustion becomes unstable, but any less retard results in knock, and the so-called “knock-stability” limit is reached. Furthermore, it is of interest to note that the results in ref. [9] shows that, for these same two datasets, the combustion efficiency increases from 93.5 to 98.5% as $\Phi_m$ increases from 0.304 to 0.412. However, this increase is non-linear with a combustion efficiency reaching a value of 96.6% at $\Phi_m$ = 0.32. Experimental conditions for these two sweeps are summarized in Table 4.

Table 4. Operating conditions for the comparison between the *RI* and the *CNL*

| | | |
|---|---|---|
| $P_{in}$ [bar] | 2.0 | |
| $\Phi_m$ [-] | 0.304 → 0.332 | 0.321 → 0.412 |
| $IMEP_g$ [bar] | 8.8 → 9.8 | 9.6 → 12.1 |
| $T_{in}$ [˚C] | 30 | |
| *RI* [MW/m$^2$] | 1.9 → 9.9 (no EGR) | ~ 5 (with EGR) |
| Engine speed [RPM] | 1200 | |
| Geometric *CR* [-] | 14:1 | |
| Fuel | Research-Grade Gasoline | |
| Fueling system | GDI with *SOI* @ 60˚CA | |

An important feature of the first $\Phi_m$ sweep (no EGR) is that the thermal efficiency (Figure 4-b) increases through a maximum of 47.6% at $\Phi_m$ = 0.320 and then drops. As explained into further details in ref. [9], this is due to a tradeoff between the following two effects:

1. With increased $\Phi_m$, combustion is hotter, resulting in improved combustion efficiency. Additionally *CA50* advances giving a small increase in the expansion ratio which tends to increase the thermal efficiency. However, this second effect is small because the expansion ratio changes only slightly when *CA50* is close to TDC, as discussed in ref. [9].
2. Heat transfer losses increase significantly as the ringing intensity increasing into the knocking regime, as discussed above and demonstrated in [8]).

As the pressure oscillations increase, the heat-transfer losses overtake the progressively smaller increase in combustion efficiency, and the thermal efficiency begins to drop [9].

By comparing Figure 4-a & -b, this maximum thermal efficiency operating point occurs for a *RI* of about 5 to 6 MW/m$^2$, which coincides well with the onset in the audible knocking characteristic noise. In addition, Figure 4-b shows that the evolution of the *KI*, which corresponds to the power content in the first resonant mode, depicts a noticeable change in the slope for *RI* ≈ 5 MW/m$^2$ (as highlighted by the two dashed linear regressions through the data). It is observed that the rate of *KI* increase becomes substantially higher as it progresses from the non-knocking to the knocking combustion regimes. Similar behavior was found by Andreae *et al.* [12], who used the substantial increase in the audible acoustic wave power to define a knock criterion on the *PPRR*. Eng suggests a *RI* limit located near the transition to higher ringing index given by a measure of the largest peak-to-peak amplitude of the band-pass filtered (first mode centered) pressure traces [11]. Thus, the additional indicator of the change in the slope of the *KI* curve, further supports the onset of knock for *RI* ≈ 5 MW/m$^2$, in addition to the drop in thermal efficiency due the substantial increase in the heat transfer induced by the knock phenomenon and the human perception of the onset of a strong knocking sound.

Concerning the second sweep (with EGR), by holding the *RI* at 5 MW/m$^2$, the *KI* variations over the sweep are much smaller than for the first sweep. Figure 4-b shows a slightly decreasing trend to the *KI* as $\Phi_m$ increases. As explained previously (see "*KI* and vibration modes" section), this could be due to the difficulty to obtain consistent information regarding the *KI* by the analysis of the power content in the first mode only. In any case, this trend is weak, and the intensity of the acoustic oscillations could be reasonably considered as constant.

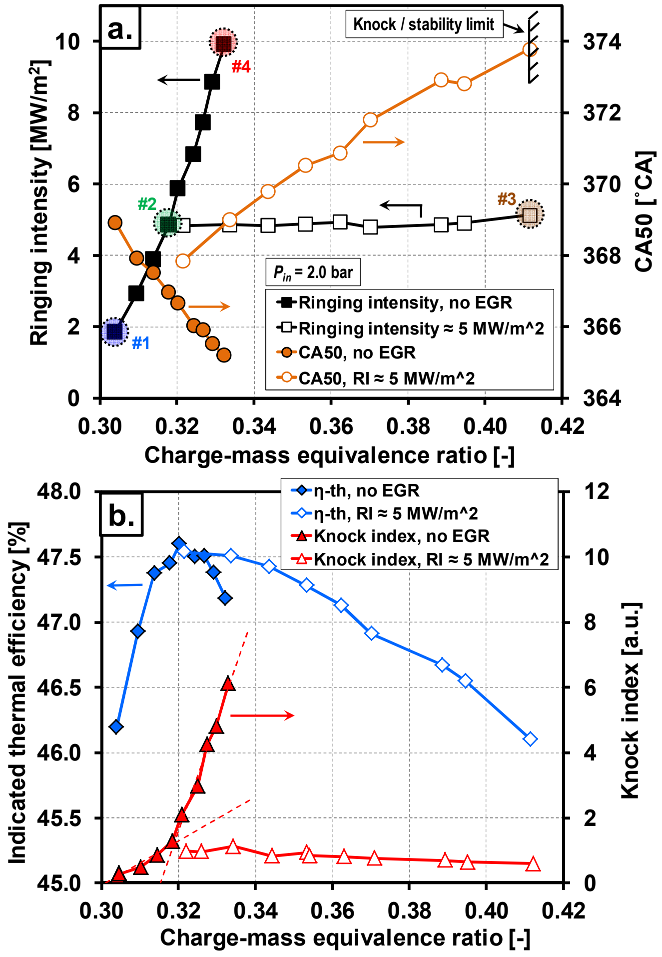

Figure 4. *RI* & *CA50* (a.) and thermal efficiency & *KI* (b.) for $\Phi_m$ sweeps for zero EGR (filled symbols) and using EGR to maintain a *RI* of ~ 5 MW/m$^2$ (empty symbols). See Table 4 for operating conditions

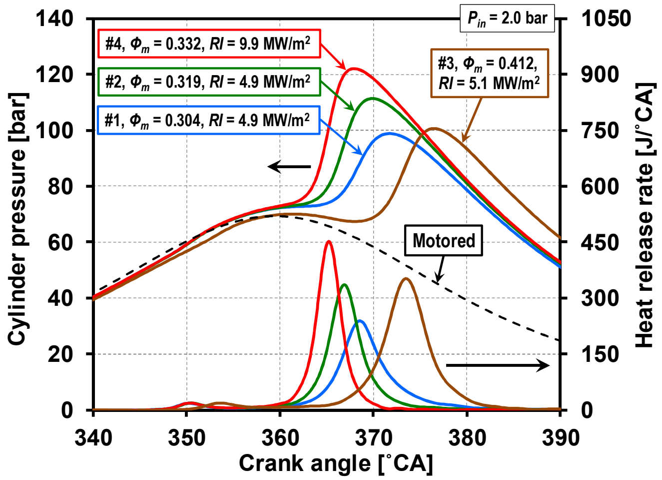

Figure 5. Low-pass filtered and ensemble averaged cylinder pressure traces and heat release rates for the four selected operating points circled (numbered from 1 to 4) in Figure 4-a.

Now that the separation between the non-knocking to knocking combustion regimes has been better identified, *RI* ≈ 5 MW/m$^2$ can reasonably be considered as a reliable threshold for the datasets presented, the response and the sensitivity of the *CNL* to the onset of engine knock will be investigated. Accordingly, Figure 6 presents the evolution of the *CNL* for the same two $\Phi_m$ sweeps. For convenience the *RI* (a measure that correlates with a pressure wave intensity has been included in the figure and is plotted on a logarithmic scale for consistency and direct comparison with the *CNL*, which is expressed in dB, a unit that is by definition a logarithmic scale. Figure 6 includes two calculations of the *CNL*: the first one results from the use of the raw pressure traces while the second uses the low-pass filtered pressure traces, as discussed below.

From these plots, it can be seen that the *CNL* follows the same trend as log(*RI*). As the *RI* rises from 1.9 to 9.9 MW/m$^2$ (no EGR sweep), the *CNL* increases from 85.4 to 94.8 dB. This general trend of the *CNL* increasing with the *RI* has also been reported by other researchers [2, 18, 22]. In addition, the second sweep in Figure 6 (with EGR) shows that the *CNL* is nearly constant when the *RI* is maintained at ~ 5 MW/m$^2$. For these datasets, a *RI* of ~ 5 MW/m$^2$ corresponds to a *CNL* of ~ 90.4 dB. However, it should be pointed out, that as other engine parameters are varied (*e.g.* $P_{in}$ and engine speed), a *CNL* of 90.4 dB does not always correspond to a *RI* ≈ 5 MW/m$^2$, as it will be shown in the next sections. Therefore, it is not possible to use the criterion of a specific *CNL* value to detect the onset of knock over a wide range of operating conditions, as is done for the *RI*.

Figure 7 presents the PSDs for the four selected operating points from Figure 4-a (also shown in Figure 6). Analysis of these PSDs reveals that as *RI* rises (operating points #1, 2 & 4), the power content increases in all modes displayed. The growing power content in all of the modes acts to increase the *CNL,* but the contribution of each mode depends on its magnitude and on its attenuation by the engine structure (represented by the gray line in Figure 7).

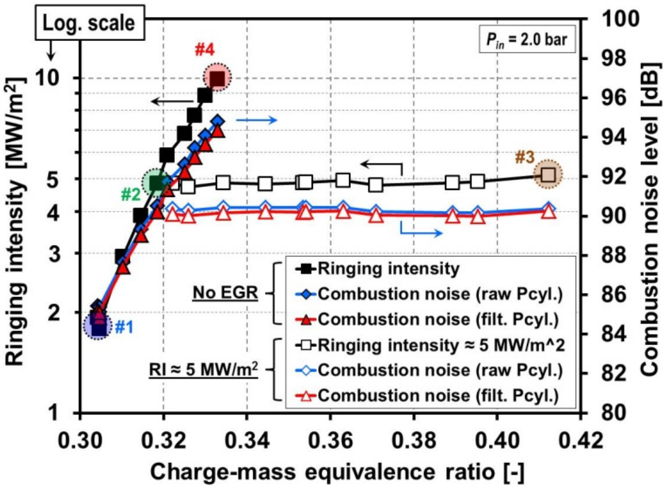

Figure 6. *RI* (log. scale) & *CNL* for $\Phi_m$ sweeps for zero EGR (filled symbols) and using EGR to maintain a *RI* of ~ 5 MW/m$^2$ (empty symbols). The *CNL* was calculated from both the raw & low-pass filtered pressure traces. See Table 4 for operating conditions.

For the second sweep, in accordance with a constant *CNL* (Figure 6), nearly identical PSDs are obtained for operating points #2 and 3, which also have the same a similar *RI* (~ 5 MW/m$^2$). However, between these two operating points, two small differences should be noted. First and most significantly, it can be seen that the power content of the first resonant mode decreases, as given by a decrease in the *KI* (as mentioned in relation to Figure 4-b). Nevertheless, the power content of the second mode does not vary significantly (only 3%). The second small difference is the shift in the location of the peaks of the first and second resonant modes for the four PSDs displayed. They shift to slightly higher frequencies as $\Phi_m$ and/or *RI* are increased. This is because of the higher temperatures with increasing $\Phi_m$, which lead to higher sound velocities.

Examination of the trends of the *CNL* curves in Figure 6 shows no indication of any distinctive change in the *CNL* slope at the transition from the non-knocking to knocking combustion regimes (*RI* ≈ 5 MW/m$^2$). This contrasts with what would be expected from the rapidly growing power content of the first mode as the engine starts knocking (see first and second mode in Figure 7 and the *KI* in Figure 4-b). It is therefore of interest to investigate the contribution of the resonant modes' power content (mainly the first and second modes) to the total *CNL* and to compare it to the *CNL* induced by the pressure rise from the "normal" combustion process included in the "zero" mode. To do so, the *CNL* computed from the raw and the low-pass filtered pressure traces are compared. As shown by dotted curves in Figure 7, the filtering process effectively truncates the frequency components induced by the ringing/knock phenomenon, while leaving the "zero" mode intact.

As seen in Figure 6, *CNL* computed from the raw and filtered pressure traces are very similar. The *CNL* computed from the raw pressure traces is slightly higher than the one from the filtered pressure trace, by 0.2 and 0.5 dB as *RI* increases from 1.9 to 9.9 MW/m$^2$. This small difference is due to the contribution of the resonant modes to the *CNL*, which increases as *RI* increases (as seen in Figure 7). As a result, it can be concluded that the resonant modes do not significantly contribute the overall *CNL*. This is explained by the much lower magnitude of the resonant modes (note the logarithmic scale in Figure 7), the fact the resonant modes' frequency ranges are more attenuated by the engine-structure filter (also displayed in Figure 7) and the logarithmic nature of the noise perceived by the human ear (this aspect will be further discussed in the next subsection).

It is important to note that although the *CNL* accounts for human-ear perception in terms of the overall sound level (the A-filter and logarithmic scale), it does not account for the human ear's ability to detect unique sounds within an overall background noise. For this reason, the human ear readily detects the characteristic sharp sound of engine knock as unpleasant/annoying even though the knock does not add significantly to the overall total noise level, *i.e.* the *CNL*. To address the quality of the sound other metrics are needed, for instance like the one developed by Payri *et al.* [34] for conventional diesel injection.

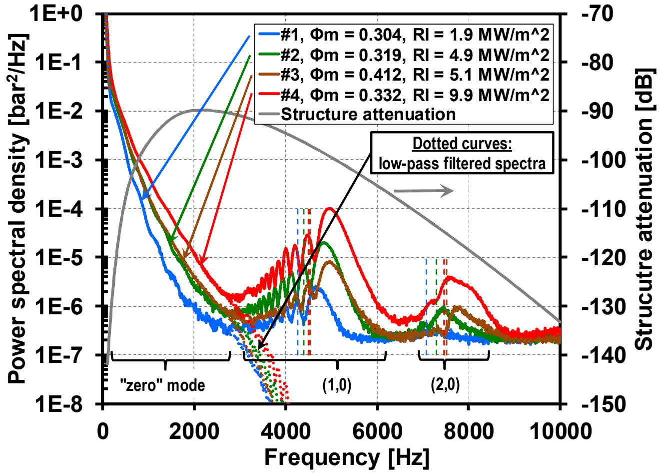

Figure 7. Raw and low-pass filtered ensemble-averaged frequency spectra for the four operating points circled (numbered from 1 to 4) in Figure 4-a and Figure 6. Straight vertical dashed lines representing the estimated first and second order mode vibration frequencies according to the solution of the wave equation for a simplified right circular cylinder (Equation 3).

It should also be mentioned that under some circumstances the resonant modes' power content could have a noticeable contribution to the *CNL*. For instance, it might be the case under unwanted high *RI* conditions (much higher than 10 MW/m$^2$), or/and for conditions for which the first mode occurs in a lower frequency range that is less attenuated by the engine structure, such as for large-bore engines.

In short, the *CNL* represents a complementary metric to the *RI* which is a metric that does correlate to the propensity of the combustion process to produce an acoustically resonating wave leading to knock. Hence, the *RI* appears to be a better criterion for the sake of combustion investigations to avoid unwanted knocking combustion regimes, while the *CNL* is valuable for determining the overall loudness of an engine, particularly the noise induced by the "normal" combustion process.

## Contribution of the Knock/Ringing Frequency Components to the Intensity of Sound

It has been found by comparing the *CNL* trend to the onset of knock and beyond (as given by a *RI* > 5 MW/m$^2$), that the overall loudness of the combustion is not significantly affected by the additional noise, emitted at higher frequencies from the resonating waves originated from the knock/ringing phenomenon. This has been explained by a combination of a lower magnitude of the resonant modes and the fact that they are located in frequency ranges that are on average more attenuated by the engine structure than the "zero" mode (induced by the main pressure rise). Moreover, once this attenuated spectral power is converted into noise (in dB), which has a logarithmic scale, the relatively small additional contribution of the resonant modes to the total *CNL* becomes insignificant.

In order to investigate the combustion noise sources, not as perceived by the human ear but as emitted by the engine structure, it is more appropriate to consider the noise on a linear scale such as the one given by the sound pressure (Pa) or intensity of sound (W/m$^2$) (Equation 4). Accordingly, Figure 8 shows the cumulative of the intensity of sound (attenuated by the engine structure and the A-filter) as a function of frequency for the operating point #2 in Figure 7 ($\Phi_m$ = 0.319, *RI* = 4.9 MW/m$^2$). This data point has been selected to analyze the sources of engine noise for a representative operating point at the onset of knock. Sound intensity values have been normalized by the corresponding total intensity of sound of 1.12 mW/m$^2$ for this operating condition, and then given in percent.

For this non-knocking case, according to Figure 8, about 92.5% of the sound power is contained in the "zero" mode between 400 and 2750 Hz. Below 400 Hz, the frequency components are strongly attenuated by the engine structure and 2750 Hz is the high-frequency limit of the "zero" mode. Moreover, the 400 Hz to 2000 Hz range comprises the majority of the total sound intensity (about 90%). This particular frequency range was found to be well representative of the *CNL* magnitude over a range of conditions, and therefore will be used in the following sections of this article to discuss the presented results. The remainder, about 7.5% of the cumulative sound intensity, corresponds to sound power percent from the ringing phenomenon (virtually all of it contained in the first mode between ~ 3000 and 5000 Hz). It represents a non-negligible power fraction of the total sound power emitted by the engine structure. However, this is not perceived significantly louder by the human ear (+ 0.3 dB) due to its logarithmic response.

Interestingly, the behavior is similar for knocking-combustion conditions for which the characteristic knocking sound is well perceived by the human ear. For instance, for the operating point #4 (*RI* = 9.9 MW/m$^2$), the percentage of the sound power from the ringing/knock phenomenon does not change significantly from the non-knocking operating point #2 described above. This is because, as *RI* is increased, not only does the power content in the ringing/knock modes increase but also the power content in the "zero" mode (see Figure 7). For this condition about 6.9% of the total sound intensity (total $I_{sound}$ = 3.00 mW/m$^2$) is included in the resonant modes (frequencies > about 2750 Hz). Although the total sound level, and therefore, resonant modes are about 2.7 times greater than for the non-knocking point #2, the resonant modes only contribute about 0.5 dB of the total *CNL,* due to the logarithmic scale, which is based on the response of the human ear. Not only are the contributions of the resonant modes small compared to the total *CNL*, but the change in this contribution from the non-knocking point #2 to the strongly knocking point #4 is only 0.2 dB, which is far too small to be detected reliably.

Consequently, the facts that 1) there is not a unique *CNL* value corresponding to the onset of knock (as *RI* ≈ 5 MW/m$^2$ does), 2) the knock resonant modes do not contribute significantly to the overall noise level, and 3) the change in the resonant mode contribution between non-knocking and strongly knocking operation is negligible are the reasons that the *CNL* is not useful for determining the knock propensity of HCCI combustion.

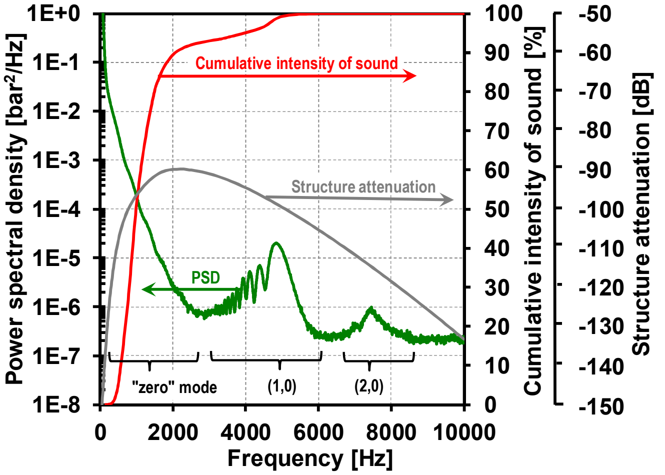

Figure 8. Power spectral density and corresponding cumulative normalized intensity of sound. Operating point #2 in Figure 7. *RI* = 4.9 MW/m$^2$, $\Phi_m$ = 0.319

## Insight into the "Zero" Mode

The analysis in the previous subsections revealed that almost all of the *CNL* could be reduced to the power content into the "zero" mode, particularly in the ~ 400 to 2000 Hz frequency range. It has also been shown by removing the resonating frequency components (applying a low-pass filter to the pressure traces) that the output is very similar to the one from the original/raw pressure trace. Hence, the *CNL* is dominated by the "zero" mode frequency components, which is induced by the main pressure rise, *i.e* compression, "normal" combustion process and expansion. It is therefore of interest to further investigate the noise sources contributing to the "zero" mode.

Figure 9 shows the PSD of operating point #2 plotted with the frequency on a log-scale to emphasize the "zero" mode. It can be seen that there is a distinct concave bend in this curve in the 100 – 300 Hz range. To understand reason for this behavior, the PSD of a comparable motored-engine pressure trace is also plotted (dashed line). It can be seen that the motored curve tracks the fired-engine curve up to the mid-point of this concave feature. For frequencies above this point, the fired-engine PSD shows significantly higher power. Thus, the region between the motored and fired curves represents the noise produced by the "normal" combustion process. If the combustion induces acoustic oscillations, as it does here, then the first- and second-order (and sometimes higher order) resonant modes are also visible at higher frequencies (*i.e.* > ~2750 Hz).

For the lower frequencies, up to around 150 to 200 Hz, a large portion of the energy contribution to the in-cylinder pressure comes from the motored signal. Similar results were obtained by Bhat *et al.* [36] and Payri *et al.* [37]. In this case, the motored noise is 73.2 dB or an intensity of sound of $4.5\times10^{-4}$ mW/m$^2$, which is 0.04% of the total sound intensity of 1.12 mW/m$^2$ (obtained by integrating the PSD over the entire frequency range and applying the attenuation filters). This very low value is because the frequency component associated with the motored signal is strongly attenuated by the engine structure (see filter curve in Figure 9). The higher-frequency contributions of the acoustic oscillations to the total sound intensity are also small, as discussed in the preceding subsection.

As a result, the power content in the region between the motored-noise and the acoustic oscillations produces most of the *CNL*. As the gray-shaded region in the figure shows, it is represented reasonably well by to 400 – 2000 Hz range discussed in the previous subsection.

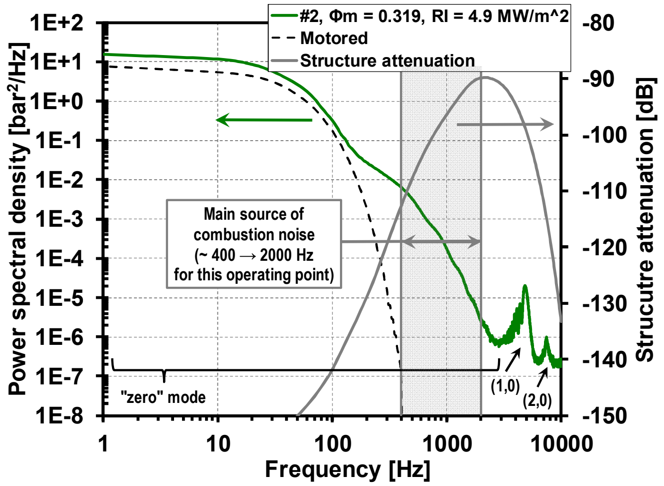

Figure 9. Comparison of the ensemble averaged PSDs between a motored case and a fired case (Operating point #2 in Figure 7. *RI* = 4.9 MW/m$^2$, $\Phi_m$ = 0.319).

## Influence of Engine Load on the CNL

Commonly, for HCCI combustion, the operating parameters are tuned so that the engine operates at or close to the knock limit (*RI* ~ 5 MW/m$^2$) with an appropriate safety margin. This is done primarily because it is advantageous to advance *CA50* as much as possible to obtain a high thermal efficiency and acceptable stability (*i.e.* $COV_{IMEPg}$ < ~ 2 %) [1, 9, 31]. However, advancing *CA50* increases the *PPRR*, which can lead to knock, so care must be taken to not exceed the allowable ringing limit (*i.e. RI* ~ 5 MW/m$^2$ in our case). This increase in the *PPRR* also increases the noise from the "normal" combustion (*i.e.* the "zero" mode in the PSD plots), which could become excessive. Controlling *CA50* to maintain good efficiency and stability, while avoiding excessive ringing and keeping noise levels acceptable is particularly challenging when varying the engine load. Therefore, it is crucial to understand and quantify how the *CNL* varies with load, especially how it behaves as the engine is approaching its high load limit for these LTC-HCCI like engines.

Variation in load can be accomplished by changing the fueling rate (changing $\Phi_m$) or the boost pressure (at constant $\Phi_m$). The influence of both parameters on the *CNL* is independently investigated in the following.

### $\Phi_m$ Effect on the *CNL*

It has been shown in the previous section that for operation at an intake pressure of 2.0 bar and holding the *RI* at about 5 MW/m$^2$, the *CNL* is nearly constant when $\Phi_m$ is varied from 0.32 to 0.41. This corresponds to an increase in the $IMEP_g$ from 9.6 to 12.1 bar. This has been attributed to the fact that the spectral energy generated by the combustion-induced cylinder pressure rise remains nearly the same within this $\Phi_m$ range and for these operating conditions. In order to study the $\Phi_m$ effect over a wider operating range, two other sweeps were performed. In Figure 10, data for two intake pressures, 1.0 and 2.4 bar are presented, with a variation of $\Phi_m$ from 0.25 to 0.44 ($IMEP_g$ = 2.5 to 5.0 bar) and 0.17 to 0.47 ($IMEP_g$ = 4.4 to 16.0 bar), respectively. To hold the *RI* constant at about 5 MW/m$^2$ (Figure 10-a), the *CA50* was controlled by either adjusting the intake temperature or the EGR rate (the latter was used for conditions where $T_{in}$ = 30˚C [7]). Some selected low-pass filtered and ensemble averaged cylinder pressure traces and heat release rates are displayed in Figure 11. These correspond to the operating points marked with colored arrows in Figure 10, for the 2.4 bar intake pressure dataset. Experimental conditions are summarized in Table 5.

Table 5. Operating conditions for the $\Phi_m$ effect on the *CNL*

| | | |
|---|---|---|
| $P_{in}$ [bar] | 1.0 | 2.4 |
| $\Phi_m$ [-] | 0.25 → 0.44 | 0.17 → 0.47 |
| $IMEP_g$ [bar] | 2.5 → 5.0 | 4.4 → 16.0 |
| $T_{in}$ [˚C] | 181 → 115<br>(no EGR) | 133 → 30 ($\Phi_m$ = 0.17 → 0.23, no EGR)<br>30 ($\Phi_m$ > 0.23, with EGR) |
| *RI* [MW/m$^2$] | ~ 5 | |
| Engine speed [RPM] | 1200 | |
| Geometric *CR* [-] | 16:1 | |
| Fuel | Certificate gasoline | |
| Fueling system | GDI with *SOI* @ 60˚CA | |

As for the narrower $\Phi_m$ sweep for *RI* ≈ 5 MW/m$^2$ presented previously in Figure 6, Figure 10-b shows that the *CNL* is nearly constant over a wide $\Phi_m$ range. For an intake pressure of 1.0 bar, the *CNL* is nearly constant at ~ 88.6 dB, from $\Phi_m$ ~ 0.30 to 0.44. For an intake pressure of 2.4 bar, the *CNL* is ~ 91.3 dB, from $\Phi_m$ ~ 0.23 to 0.47. For both intake pressures, the

---

[7] EGR is the control method chosen for conditions where additional *CA50* retard was required after $T_{in}$ was reduced to 30°C since $T_{in}$ cannot be reduced below this value in a practical manner.

highest $\Phi_m$ reached correspond to the knock/stability limit [25, 38, 39]. The substantial increase in the *CNL* (by ~ 2.7 dB) between the two intake pressures will be discussed in detail in the next subsection. Toward the low $\Phi_m$ side, the *CNL* gradually decreases for both sweeps. At $P_{in}$ = 1.0 bar, it decreases to 87.3 dB (- 1.3 dB) as $\Phi_m$ is decreased to 0.25, and at $P_{in}$ = 2.4 bar, it decreases to 89.3 dB (- 2.0 dB) as $\Phi_m$ is decreased to 0.17. It should be pointed out that for $P_{in}$ = 2.4 bar, the *RI* was not perfectly maintained at 5 MW/m$^2$. It actually slowly decreases to 4.5 MW/m$^2$ for lower $\Phi_m$, Figure 10-b). Thus, for low $\Phi_m$ the *CNLs* are slightly undervalued. As shown at $P_{in}$ = 1.0 bar and according to sensitivity of the *CNL* against the *RI* from Figure 6, it is estimated that the *CNL* should decrease by about 1.3 dB as $\Phi_m$ decreases to 0.17 for $P_{in}$ = 2.4 bar, if the *RI* was held stable.

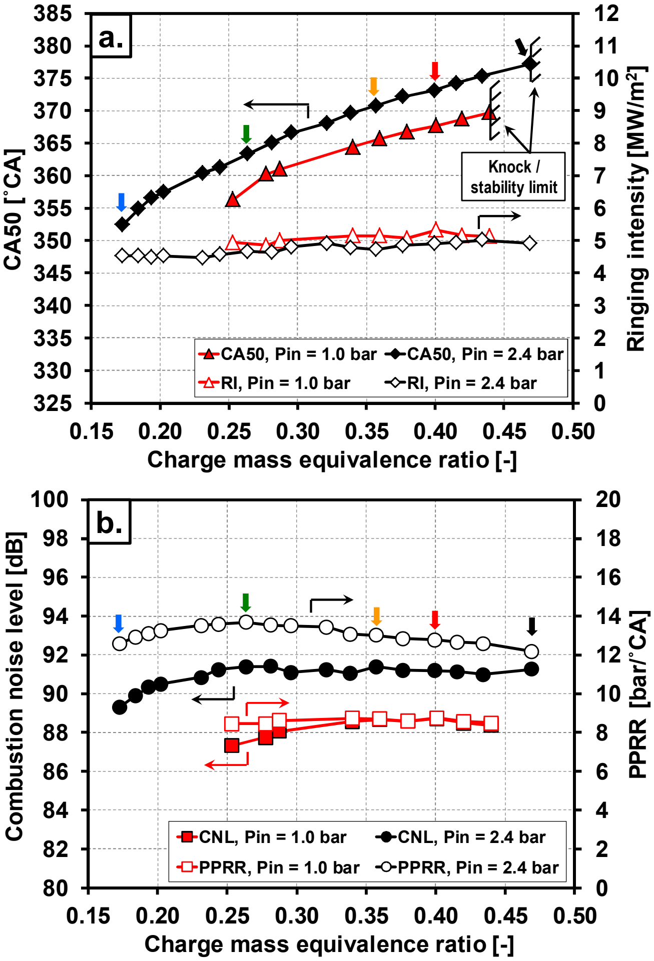

Figure 10. *CA50* & *RI* (a.) and *CNL* & *PPRR* (b.) as a function of $\Phi_m$ for two $P_{in}$ (1.0 and 2.4 bar). See Table 5 for the operating conditions.

Maintaining the *RI* ~ 5 MW/m$^2$ over these wide $\Phi_m$ ranges, required considerable *CA50* variation. It can be seen in Figure 10-a that the decrease in the *CNL* in the low $\Phi_m$ side, corresponds to *CA50* close to or before TDC. It should also be mentioned that combustion phasings before TDC are not usually desirable for practical HCCI operation, due to the negative work which impedes the thermal efficiency. In this study, they were performed for the sake of covering a larger $\Phi_m$ range, for an improved understanding.

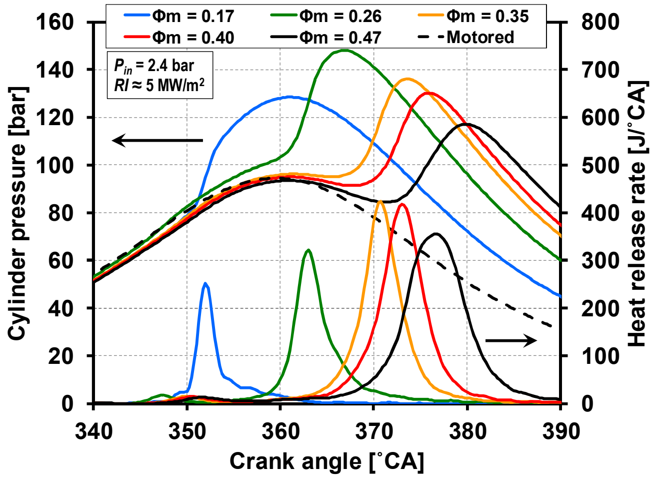

Figure 11. $\Phi_m$ effect on the cylinder pressure traces (low-pass filtered and then ensemble averaged) and heat release rates for some selected operating points marked by colored arrows in Figure 10, $P_{in}$ = 2.4 bar. *CA50* is more retarded with $\Phi_m$ to maintain *RI* ≈ 5 MW/m$^2$.

These trends in the *CNL* as a function of $\Phi_m$, can be explained by the magnitude of the “zero” mode as illustrated on Figure 12 for $P_{in}$ = 2.4 bar. It can be seen in this figure that the PSDs for $\Phi_m$ = 0.26 and 0.47 are quite similar in the ~ 400 to 2000 Hz frequency range, resulting in similar *CNLs*. Moreover, in agreement with a decrease in the *CNL* for low $\Phi_m$ (or *CA50* <≈ TDC), the PSD for $\Phi_m$ = 0.17 exhibits a lower magnitude in the ~ 400 to 1000 Hz range.

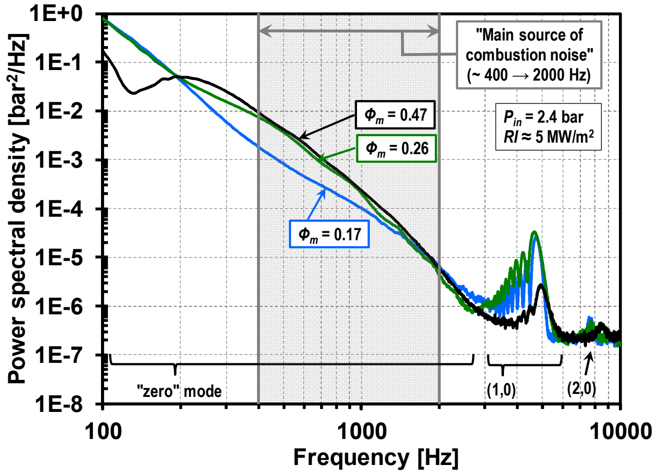

Figure 12. $\Phi_m$ effect on the ensemble-averaged PSDs for three selected operating points marked by colored arrows in Figure 10, $P_{in}$ = 2.4 bar, *RI* ≈ 5 MW/m$^2$.

It was shown in the previous section that variations in the power content in the ~ 400 to 2000 Hz range are induced by the changes in the pressure trace due to the “normal” combustion process (the contribution of the motored and the acoustic oscillations can be neglected). As a first-order approximation, it can be postulated that the magnitude of the higher frequency components in the “zero” mode are related to the *PRR*, for a higher *PRR*, a higher power content in the “zero” mode would be expected. For simplicity, the *PRR,* whose magnitude varies through the combustion event is often reduced to the *PPRR*.

However, comparing the *CNL* and the *PPRR* in Figure 10-b, shows that the *PPRR* trend alone does not entirely explain the *CNL* results. For instance, at $P_{in}$ = 2.4 bar, for 0.25 ≤ $\Phi_m$ ≤ 0.47, the *PPRR* slightly decreases [8] (from ~ 13.7 to 12.3 bar/˚CA) while the *CNL* remains essentially constant at ~ 91.3 dB. The opposite statement could be made for $P_{in}$ = 1.0 bar, where the *PPRR* is about constant (~ 8.6 bar/˚CA) but the *CNL* decreases at low $\Phi_m$ (~ 88.6 to 87.3 dB). This means that the *PPRR* alone does not seems to provide sufficient information to represent the power content in the "zero" mode (*i.e.* mainly between ~ 400 and 2000 Hz), and thus, the changes in *CNL* when $\Phi_m$ is independently varied. As it will be shown in the next subsection, *PPRR* does correlate well with the *CNL* while other engine parameters are varied. It is thought that there might be a complex interaction between variations in the shape of the pressure trace as $\Phi_m$ is varied (particularly during the combustion event) that affect the its corresponding frequency spectra in the ~ 400 to 2000 range. Fully understanding this would require a detailed investigation, which is beyond the scope of the present study.

## $P_{in}$ Effect on the *CNL*

To investigate the influence of the boost pressure on the *CNL*, *CA50* sweeps (which also sweep the *RI*) were conducted at four intake pressures (1.0, 1.3, 1.6 and 2.0 bar) at a constant $\Phi_m$ of 0.40 (Figure 13). The $P_{in}$ effect on the cylinder-pressure traces and the corresponding *HRRs* are provided in Figure 14, for the operating points at a *RI* of about 2.3 MW/m$^2$ (operating points marked with the colored arrows in Figure 13). On average, the $IMEP_g$ increases from about 4.1 to 9.8 bar as $P_{in}$ is increased from 1.0 to 2.0 bar [9]. Experimental conditions are summarized in Table 6.

Table 6. Operating conditions for the $P_{in}$ effect on the *CNL*

| $P_{in}$ [bar] | 1.0 | 1.3 | 1.6 | 2.0 |
|---|---|---|---|---|
| $\Phi_m$ [-] | 0.40 | | | |
| $IMEP_g$ [bar] | ~ 4.1 | ~ 5.7 | ~ 7.9 | ~ 9.8 |
| $T_{in}$ [˚C] | 152<br>(with EGR) | 130<br>(with EGR) | 80<br>(with EGR) | 60<br>(with EGR) |
| *RI* [MW/m$^2$] | 0.1 → 6.2 | 0.2 → 13.4 | 0.9 → 12.5 | 0.9 → 8.3 |
| Engine speed [RPM] | 1200 | | | |
| Geometric *CR* [-] | 14:1 | | | |
| Fuel | Research-Grade Gasoline | | | |
| Fueling system | Premixed | | | |

As $P_{in}$ was increased, the intake temperature was progressively reduced from 152 to 60˚C [10], as shown in Table 6, in order to partially compensate for the effects of increased $P_{in}$ which tend to enhance autoignition and advance the *CA50*, causing an increase the *PRR* [1, 40]. For each $P_{in}$, the intake temperature was held constant, and the *CA50* sweep was performed by varying the amount of EGR (Figure 13). The charge mixture reactivity increases as the EGR amount is reduced, which results in a more advanced *CA50* and an increase in the *RI*, as can be seen in Figure 13.

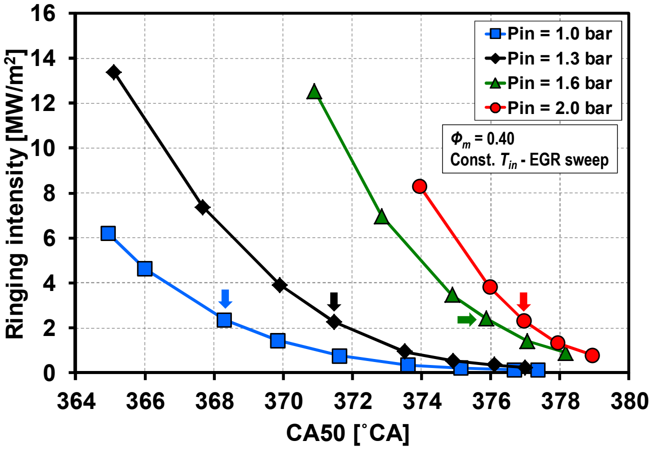

Figure 13. Influence of the $P_{in}$ on the relationship between the *RI* and the *CA50*, $\Phi_m$ = 0.40. See Table 6 for the operating conditions.

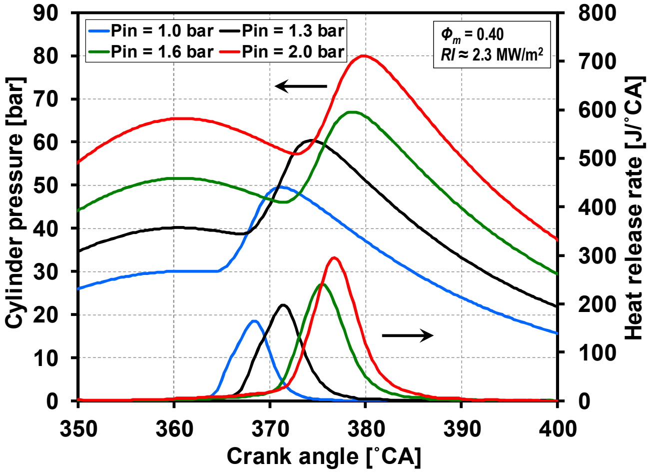

Figure 14. $P_{in}$ effect on the cylinder pressure traces (low-pass filtered and then ensemble averaged) and heat release rates for four selected operating points marked by colored arrows in Figure 13, $\Phi_m$ = 0.40. The *CA50* is retarded as $P_{in}$ increases to maintain *RI* ≈ 2.3 MW/m$^2$.

It of interest to note that the *PPRR* required to obtain a constant *RI* increases with increased $P_{in}$ (for a constant $\Phi_m$). This occurs because the peak pressure increases with boost and the maximum temperature decreases, as will be discussed for the *RI* ≈ 2.3 MW/m$^2$ points denoted by the arrows in Figure 13. Figure 13 shows that *CA50* must be retarded with increased boost to maintain a constant *RI*. Although this mitigates the increase in peak pressure with increased $P_{in}$, the peak pressure still increases from ~ 50 to 80 bar as $P_{in}$ is increased from 1 to 2 bar, as shown in Figure 14. Additionally, the required *CA50* retard, in combination with the use of a lower intake temperature (Table 6), causes a decrease in the peak mass-average temperature from 1832 to 1652 K. Referring to the *RI* equation (Equation 3), these changes in the

---

[8] To maintain a constant *RI* ≈ 5 MW/m$^2$, *PPRR* must drop slightly while $P_{max}$ decreases (see Equation 2)

[9] For each $P_{in}$, the *CA50* also affects $IMEP_g$ through its effect on the thermal efficiency.

[10] For these premixed data, operating points were not acquired for $T_{in}$ < 60°C since condensation of the pre-vaporized fuel was considered likely.

peak pressure and temperature require that the *PPRR* be higher to obtain the same *RI*. Thus, increasing $P_{in}$ for a constant *RI* allows a higher *PPRR*. For the $RI \approx 2.3$ MW/m$^2$ points in Figure 13 and Figure 14, the *PPRR* increases from 3.8 to 4.9 bar/˚CA.

Figure 15 compares the log(*RI)* and the *CNL* for the four $P_{in}$ datasets in Figure 13. It can be seen that the *CNL* increases by ~ 2.2 dB as $P_{in}$ increases from 1.0 to 2.0 bar, for any *RI* for which the comparison is possible (~ 0.8 to 7 MW/m$^2$). These results are in accordance with the one presented earlier in Figure 10-b, for which the *CNL* increased by 2.7 dB as $P_{in}$ increased from 1.0 to 2.4 bar, over a large $\Phi_m$ range (0.25 to 0.44). Moreover, as noticed in Figure 6, the *CNL* in Figure 15 significantly increases with the *RI*. The increase in the *CNL* with *RI* and boost pressure is attributed to higher magnitude of the "zero" mode, as discussed above. The change in the "zero" mode for increased boost pressure at a constant $RI \approx 2.3$ MW/m$^2$ is shown in Figure 16.

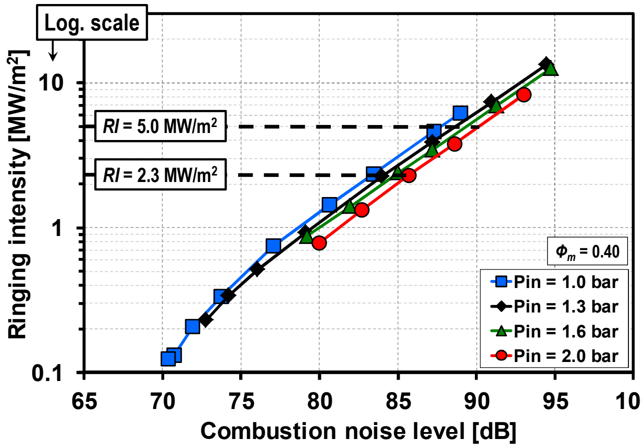

Figure 15. Relationship between the *RI* and the *CNL* for four $P_{in}$. A *CA50* (or *RI*) sweep was performed for each of the $P_{in}$, $\Phi_m = 0.40$. See Table 6 for the operating conditions.

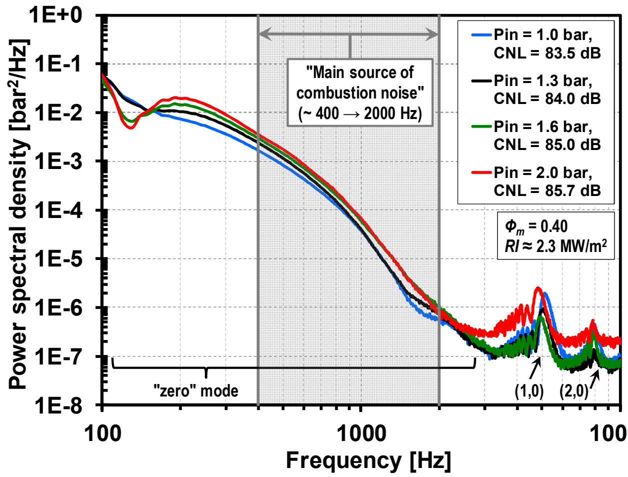

Figure 16. $P_{in}$ effect on the ensemble-averaged PSDs. Operating points are marked by colored arrows in Figure 10, $\Phi_m = 0.40$, $RI \approx 2.3$ MW/m$^2$. The magnitude of the PSD increases as $P_{in}$ increases.

As explained above, for a constant *RI*, the *PPRR* increases with increasing $P_{in}$. Thus, the behavior of the *PPRR* and the *RI* with increasing $P_{in}$ are not the same. With this in mind, the *CNL* data from Figure 15 are repotted against *PPRR* in Figure 17. As can be seen, the *CNL* data for the different $P_{in}$ collapse when they are plotted against *PPRR* rather than *RI*. Thus, increasing the *PPRR* through an increase in the *RI* at constant $P_{in}$, has a similar effect on the *CNL* to increasing the *PPRR* through an increase in the $P_{in}$ at a constant *RI*. Furthermore, this result suggests a close coupling between *PPRR* and *CNL*. However, this latter finding should be applied with caution since the coupling between *PPRR* and *CNL* is not always so close. For example, it was found in the previous subsection that when $\Phi_m$ is varied at constant boost and *RI*, the correlation between *PPRR* and *CNL* was not as good (Figure 10-b). The reason for this discrepancy between the datasets is not completely understood and requires further investigation. As previously mentioned, it is expected that the complete history of the pressure changes due to combustion (explaining the power content in the ~ 400 to 2000 Hz range of the PSD) might be involved, not just the *PPRR*.

Finally, the increase in the *CNL* with $P_{in}$ shown in Figure 15 could be compensated for by a decrease in the *RI*. For instance, as $P_{in}$ is increased from 1.0 and 2.0 bar, the *CNL* is increased by 2.2 dB if *RI* is held constant. However, $P_{in}$ could be increased over this same range with no increase in *CNL* if *RI* was decreased from 5 to ~ 3 MW/m$^2$.

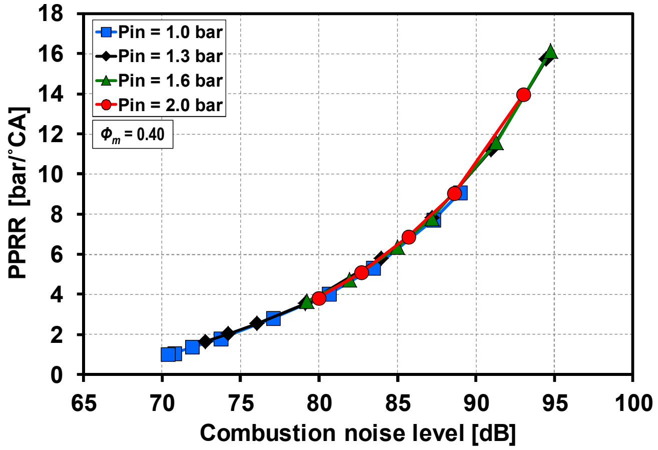

Figure 17. Relationship between the *PPRR* and the *CNL* for the four $P_{in}$. A *CA50* (or *RI*) sweep was performed for each of the $P_{in}$, $\Phi_m = 0.40$. See Table 6 for the operating conditions.

## *Influence of Engine Speed on the CNL*

In this section, the influence of engine speed on the *CNL* is investigated. Results from the literature show that the *CNL* increases with engine speed. For instance, Sellnau *et al.* [2] reported an increase from ~ 88.0 to 97.5 dB at $RI \approx 5$ MW/m$^2$, for a variation in the engine speed from 1500 to 2500 RPM. Over the same speed range and same *RI*, Shahlari *et al.* [18] found a weaker increase in the *CNL* from 91.4 to 95.8 dB. However, the focus of these two works was not to conduct well-controlled parametric sweeps, and it is unclear how the other engine parameters (such as $P_{in}$ and $\Phi_m$) were controlled during these speed sweeps.

In the current study, measurements were made at four engine speeds (600, 1200, 1800 and 2400 RPM), at a fixed intake pressure and equivalence ratio ($P_{in} = 2.0$ bar and $\Phi_m = 0.30$).

For each engine speed, a *RI* / *CA50* sweep was conducted, similar to the previous section. Experimental conditions are summarized in Table 7. In the following, first, the influence of engine speed on the behavior of the *RI* is analyzed; then, the engine speed effect on the *CNL* is presented.

Table 7. Operating conditions for the engine speed effect on the *CNL*

| | | | | |
|---|---|---|---|---|
| $P_{in}$ [bar] | 2.0 | | | |
| $\Phi_m$ [-] | 0.30 | | | |
| $IMEP_g$ [bar] | ~ 8.2 | ~ 9.1 | ~ 8.9 | ~ 7.7 |
| $T_{in}$ [˚C] | 40<br>(with EGR) | 40<br>(with EGR) | 40<br>(with EGR) | 67<br>(no EGR) |
| *RI* [MW/m$^2$] | 2.7 → 5.8 | 2.7 → 5.7 | 2.3 → 5.8 | 2.0 → 5.7 |
| Engine speed [RPM] | 600 | 1200 | 1800 | 2400 |
| Geometric *CR* [-] | 16:1 | | | |
| Fuel | Certificate gasoline | | | |
| Fueling system | GDI with *SOI* @ 60˚CA | | | |

Figure 18 illustrates the speed effect on the cylinder pressure traces for a *RI* of about 5 MW/m$^2$. For each speed, both the raw and corresponding low-pass filtered pressure traces from a selected single cycle [11] are presented. The chosen cycles are representative of the ensemble-average cycle by approximately matching the *CA50* and the *PPRR*. As observed in this figure, the peak-to-peak amplitude of the ripples significantly increases (from 1.2 to 4.6 bar [12]) as the engine speed increases from 600 to 2400 RPM. This indicates that the magnitude of the acoustic oscillations increase with engine speed despite a constant *RI* (~ 5 MW/m$^2$). Thus, the *RI* (Equation 2) might not accurately indicate the onset of knock for changes in engine speed. This increase in acoustic-oscillation magnitude at constant *RI* occurs even though the *RI* correlation includes an engine speed scaling by using *dP/dt* (time-based *PPRR*) instead of using *dP/dθ* (CA-based *PPRR*). Indeed, examination of Figure 18 shows that the CA-based *PPRR* sharply decreases (from 26.3 bar/˚CA at 600 RPM to 5.5 bar/˚CA at 2400 RPM) because of this accounting for the increase in engine speed. This corresponds to time-based *PPRRs* of 94.6 and 79.7 bar/ms, respectively. The time-based *PPRR* decreases due to the fact that the peak pressure significantly decreases with engine speed as shown in Figure 18. Nevertheless, these results indicate that the engine speed adjustment in the *RI* correlation is not sufficient to account for the actual engine-speed effect on the knock propensity, and that a greater reduction in *PPRR* with speed seems to be required.

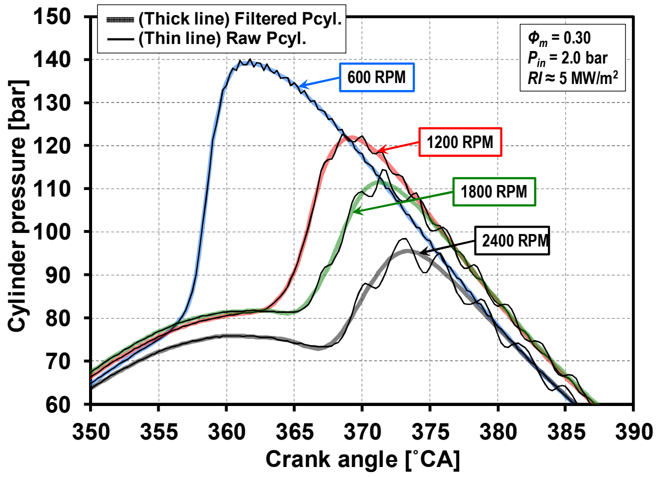

Figure 18. Representative raw and corresponding low-pass filtered single cycles (*CA50* and *PPRR* approximately match the ensemble average values) for several engine speed at *RI* ≈ 5 MW/m$^2$, $P_{in}$ = 2.0 bar, $\Phi_m$ = 0.30.

During the development of Eng's correlation [11], the engine speed effect was validated between 1000 to 3000 RPM. A good correlation was found between the largest peak-to-peak amplitude of first-mode band-pass filtered pressure signal and the *RI* calculated from Equation 3. The reasons for the discrepancy with our results are not fully understood. However, the assumption of using the peak values for the mass-average temperature, pressure, and *PRR* in the *RI* correlation, might fail under certain conditions. The use of these values by Eng [11], was based on the observation that the pressure oscillations began to appear just after the peak cylinder pressure and the assumption that they are triggered by the *PPRR*. Using the peak cylinder pressure and mass-averaged temperature appears to be reasonable at 600 and 1200 RPM since the oscillations (ripples) begin after the *PPRR* near the time of peak pressure and temperature, as evident in Figure 18. However, at 1800 and 2400 RPM, it can be seen that the pressure oscillations occur soon after the start of the main ignition, even before the *PPRR*. Under these conditions the cylinder pressure and mass-averaged temperatures are significantly lower. If these values were use in the *RI* equation instead of the peak values, it can be shown that the *PPRR* for *RI* = 5 MW/m$^2$ would be slightly lower. Consequently, the amplitude of the ripples would be smaller, but this effect is not sufficient to explain the observation in Figure 18 [13]. Furthermore, challenges reside in the detection of the cylinder pressure at the onset of the pressure oscillations and the corresponding mass-averaged temperature. Moreover, for the engine speeds of 1800 and 2400 RPM, the acoustic oscillations are excited before the *PPRR*. Therefore, it seems that there is also an uncertainty in the choice in the *PRR* to be implemented in the *RI* equation. Finally, the use of a constant *β* coefficient (see *RI* subsection for further details) might be questionable, as has been criticized by Maria *et al.* [32] and

---

[11] Single-cycle traces are used here so that the acoustic pressure oscillations are not smoothed by the ensemble-averaging operation.

[12] These values do not directly correspond to the largest peak-to-peak amplitude as observed in Figure 18, represented by a single cycle. The values are ensemble-averages of the largest peak-to-peak amplitude of each individual cycle.

[13] As shown by Equation 2, for a constant *RI*, the lower pressure would reduce the *PPRR*, while the lower temperature would act to increase the *PPRR*; however, even though this increase goes only as the square root of the temperature, the temperature at the beginning at the combustion is much lower than the peak temperature. The effect of reduced pressure still dominates, but is strongly attenuated by the reduced temperature effect, resulting in only a slightly lower *PPRR*.

Hyvönen *et al.* [33]. Further investigation, beyond the scope of this article, would be needed to address the impact of knock for higher engine speeds and also the validity of the *RI* equation to predict the onset of knock at a given *RI*, under a wide range of engine speeds.

As a result, in the following, it was preferred to use the *PPRR* as a more robust metric to analyze the speed effect on the *CNL*. This is expected to have only a minor impact on the interpretation of the subsequent results because it was shown in the first section of the results that the contribution to the *CNL* of the first resonant mode (related to the ringing phenomenon) is negligible. Moreover, it was shown that the *CNL* better correlates with the *PPRR* than the *RI*.

Figure 19 presents the influence of the engine speed on the *CNL*. Also shown are the lines for constant *RI* of 3 and 5 $MW/m^2$. It is observed that the *CNL* significantly increases with the engine speed. For instance, at a *PPRR* of 80 bar/ms [14], the *CNL* increases from 84.4 to 96.7 dB, from 600 to 2400 RPM. It is also evident that the spacing between the data curves at the various engine speeds is unequal. This indicates that the slope of the increase in the *CNL* with engine speed decreases as the engine speed increases. For example, for a *PPRR* of 80 bar/ms, the slope is 9.0 dB / 1000 RPM between 600 and 1200 RPM, but only 4.8 bar / 1000 RPM between 1800 and 2400 RPM.

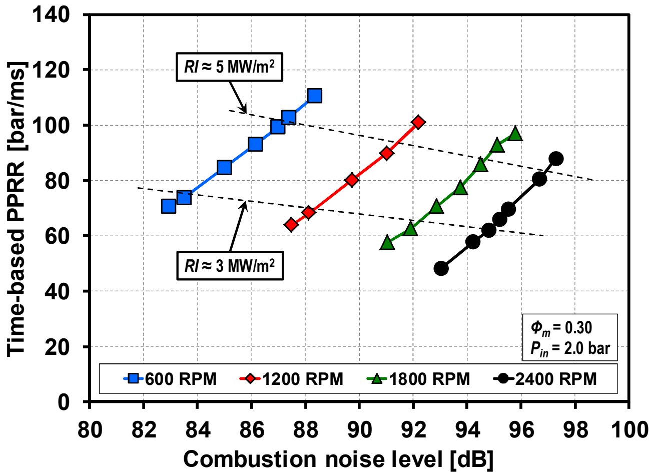

Figure 19. Relationship between the time-based *PPRR* and the *CNL* for different engine speeds. A *CA50* sweep was conducted for each engine speed. $P_{in}$ = 2.0 bar, $\Phi_m$ = 0.30. See Table 7 for the operating conditions.

As for the other datasets presented earlier, Figure 20 shows that the increase in the *CNL* with engine speed for a *PPRR* = 80 bar/ms corresponds well to a net increase in the magnitude of the "zero" mode power content in the ~ 400 to 2000 Hz range. It is therefore of interest to understand the reason of a higher magnitude of the "zero" mode when engine speed is increased.

Referring to the *CNL* calculation methodology (see the section on "Data Analysis" and Ref. [18]), engine speed information is needed to derive the frequency vector during the FFT operation. As the engine speed increases, the duration of the cycle decreases (*t* [s] = 120 / RPM for a four-stroke engine). Moreover, even though the computation is carried out on each individual single cycle, the FFT operation assumes by definition that the input signal (*i.e.* the pressure trace of each individual cycle) repeats periodically. Due to the shorter cycle time with increased speed, the combustion event and the motored-engine effects repeat more frequently. Considering an example of two pressure traces acquired at different engine speeds, but characterized by a similar time-based pressure rise, the spectral content from the combustion would be shifted to higher frequencies at higher engine speed because the combustion-induced pressure rise repeats more frequently.

Accordingly, a shift in the power spectral density to higher frequencies is evident from a comparison of the curves for the four different speeds in Figure 20 in the 400 – 2000 Hz portion of the "zero" mode. As discussed earlier in conjunction with Figure 9, this spectral range includes most of the power from the combustion event. Note that the curves are not exactly self-similar since they have been derived from real-engine data at constant *PPRR* ≈ 80 bar/ms, and the pressure-rise traces will not match exactly for the different engine speeds [15]. Nevertheless, the curves' shapes are not greatly different, and as they shift to higher frequencies, it can be seen in Figure 20 that the total power content in the 400 – 2000 Hz range increases, causing the higher *CNL* with higher speeds.

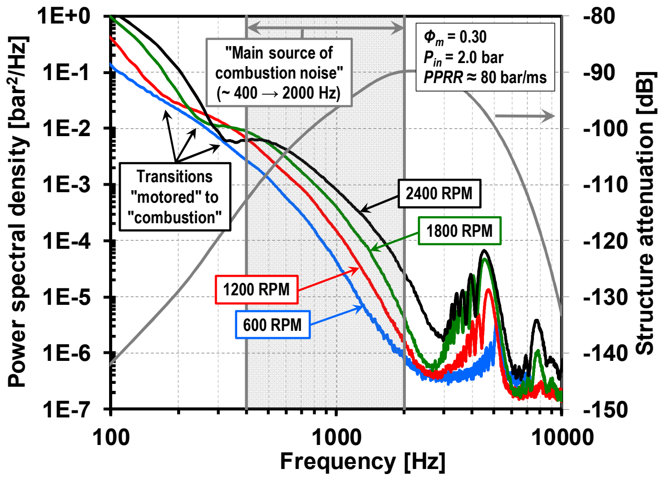

Figure 20. Influence of the engine speed on the frequency spectra (ensemble-average) for a *PPRR* ≈ 80 bar/ms, $P_{in}$ = 2.0 bar, $\Phi_m$ = 0.30. The transitions from "motored" to "combustion" correspond to feature identified in conjuncture with Figure 9.

It is also interesting to note that the transition from "motored" to "combustion" noise, marked by the concavity on the PSD curves (as explained with respect to Figure 9), also shifts to higher frequencies with increased speed (see Figure 20). This would be expected for the same reasons discussed above with respect to the repeat frequency of the combustion event. Finally, Figure 20 shows that acoustic resonance frequencies associated with knock are unchanged with engine speed, as

---

[14] This corresponds to 22.2 bar/˚CA at 600 RPM and 5.6 bar/˚CA at 2400 RPM.

[15] If the combustion pressure-rise traces were exactly self-similar in crank-angle space, the power spectral density curves for the different speeds in Figure 20 should also be self-similar, but offset to higher frequencies at higher speeds as discussed.

expected, since they are the result of the frequency of the ripples on the pressure trace, not the cycle-repeat frequency.

Finally, a comparison is performed between the increase on sound intensity (*i.e.* the *CNL* expressed in a linear scale, $I_{sound}$ as defined by Equation 4) with engine speed and the expected increase in sound intensity with engine speed based on a theoretical simplistic approach. This simple approach is based on the idea that the combustion noise, expressed on a linear scale should be proportional to the engine speed. That is, if the combustion sequence is identical, but just repeats at a different rate, the total noise should increase directly with the number of combustion events per unit time (*i.e.* the engine speed). Figure 21 presents the evolution of the measured $I_{sound}$ as a function of engine speed at a constant time-based *PPRR* of 80 bar/°CA (see Figure 19). $I_{sound}$ was calculated from the low-pass filtered pressure traces in order to discard the contribution of the first resonant mode [16]. Therefore, the $I_{sound}$ presented in Figure 21 corresponds to the sound intensity emitted by the "normal" combustion process only. The dashed line represents a proportional increase in the $I_{sound}$ with engine speed, with a reference taken at 1200 RPM (our baseline engine speed). For instance, $I_{sound}$ = 0.72 mW/m$^2$ at 1200 RPM. Therefore, according to this simple approach, $I_{sound}$ = 1.44 mW/m$^2$ at 2400 RPM (twice the $I_{sound}$ at 1200 RPM as the engine speed is multiplied by 2).

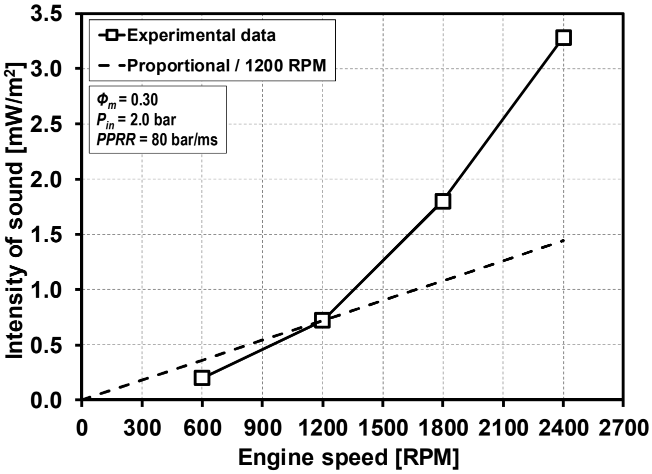

Figure 21. Intensity of sound as a function of engine speed. The dashed line to a proportional increase in the $I_{sound}$ with engine engine speed passing through the reference engine speed of 1200 RPM, $\Phi_m$ = 0.30, $P_{in}$ = 2.0 bar, *PPRR* = 80 bar/ms.

It can be seen from this figure that the $I_{sound}$ does not follow this simple approach. The measurements show a faster rate of the increase in the $I_{sound,}$ particularly for the higher speeds. This behavior might be explained by the fact that as the engine speed increases, in addition to the increase in the magnitude of frequency components in the ~ 400 to 2000 Hz range, a greater portion of the total power occurs at higher frequencies that are less attenuated by the engine structure (Figure 20). Consequently, the rate of the increase in the $I_{sound}$ is higher than if the attenuation was constant over the frequency range of interest. Additionally, the shape of the combustion pressure rise is not self-similar for the various engine speeds, which will also affect the comparison with the simple proportional approach.

## Summary & Conclusions

The origin and the sources of the HCCI combustion-generated noise were investigated in a fundamental manner. For this purpose, two commonly used cylinder-pressure derived parameters have been compared, the Combustion Noise Level (*CNL*) and the Ringing Intensity (*RI*), along with spectral analyses of the cylinder pressure traces. The *RI* was obtained according the correlation of Eng [11], for which a criterion of *RI* = 5 MW/m$^2$ was defined to set a boundary between the non-knocking and the knocking combustion regimes. The *CNL* was estimated from a spectral processing of the pressure traces. This study has been conducted on the analysis of the in-cylinder pressure traces recorded from a single cylinder HCCI research engine (~ 1 liter displacement) over a wide range of practical operating conditions.

In particular, this study focused on the sensitivity of the *CNL* to the ringing/knock phenomenon, to which the human hearing system is quite sensitive. The effects of independently varying engine operating conditions such as fueling rate ($\Phi_m$ = 0.17 to 0.47), boost pressure (100 to 240 kPa), and speed (600 to 2400 RPM) on both the *CNL* and *RI* were also investigated.

The following results were produced from this study:

<u>Regarding the validity of the *RI* correlation:</u>

1. For a given dataset ($P_{in}$ = 2.0 bar, $\Phi_m$ sweep, 1200 RPM), the criterion *RI* = 5 MW/m$^2$ was confirmed to be a reliable indicator of the onset of significant ringing (*i.e.* onset of knock) as shown by a substantial increase in the *KI*, a drop in the thermal efficiency due to an additional increase in the heat-transfer losses, and the subjective human perception of the onset of a distinctive sharp knocking sound. The *RI* also appeared to be a good indicator of knock for changes in boost pressure and combinations of changes in boost pressure and fueling rate ($\Phi_m$).

2. Despite a constant *RI*, the amplitude of the ripples on the pressure trace increased as engine speed was increased. This indicates that the *RI* correlation might not accurately indicate the onset of knock for changes in engine speed. Further investigation, would be required to address the impact of the knocking phenomenon for higher engine speeds and the validity of the *RI* equation to predicting the onset of knock, under a wide range of engine speeds.

<u>Regarding the sources of the *CNL*:</u>

3. The magnitude of the *CNL* was found to be effectively represented by the power content in the "zero" mode, particularly in the ~ 400 to 2000 Hz range, for the conditions investigated in this study. This frequency range corresponds to the contribution of the combustion process to the pressure rise, with no significant contribution from any acoustic resonant modes.

---

[16] In this case, the aim is to separately study the effect of the "normal" combustion process on the increase in $I_{sound}$ with engine speed. However, as discussed in relation to Figure 8, the $I_{sound}$ induced by the first resonant mode could contribute significantly to the total $I_{sound}$.

4. It was found that the *CNL* is not useful for determining the knock propensity of HCCI combustion for the following two reasons:
    a. First, the *CNL* is not sensitive to the power content of the ringing/knock resonant modes. This is explained by the significantly lower magnitude of the resonant modes compared to the “zero” mode. Moreover, the higher frequencies of the resonant modes are more attenuated by the engine structure. Finally, since the base-noise (induced by the “normal” combustion process) is already relatively high, the logarithmic nature of the noise perceived by the human ear attributes only an almost negligible increase in the *CNL* to the additional noise induced by the knock phenomenon.
    b. Second, the onset of knock does not correspond to a fixed value of the *CNL*. Indeed the *CNL* was found to significantly vary with engine operating parameters ($\Phi_m$, $P_{in}$, and engine speed) for constant *RI* (*i.e.* 5 MW/$m^2$).

5. It was observed that the *CNL* generally correlates well with the Peak Pressure Rise Rate (*PPRR*), particularly when either the *RI* or the $P_{in}$ is varied at a given $\Phi_m$. However, the correlation between *PPRR* and *CNL* did not correlate well when $\Phi_m$ was independently varied for boosted conditions (*CNL* was nearly constant while *PPRR* decreased about 15% with increasing $\Phi_m$ over the wide $\Phi_m$ range investigated). To explain this behavior, further investigation would be required to understand the effects of more detailed changes in the pressure trace than just the changes in the *PPRR*.

Regarding the effect of engine load on the *CNL*:

6. At a fixed $P_{in}$ and *RI* (5 MW/$m^2$), the *CNL* was found to be nearly constant over a wide representative $\Phi_m$ range, from low loads up to the knock/stability limit. Therefore, increasing the engine load through $\Phi_m$ represents an efficient way for obtaining higher loads without a noise penalty.

7. At fixed $\Phi_m$, for a large range of practical *RI* levels, the *CNL* increases with the boost pressure (+ ~ 2.2 dB for a $P_{in}$ variation from 1.0 to 2.0 bar). This increase in the *CNL* could be mitigated by decreasing the *RI* with more *CA50* retard. However, when increasing *CA50* retard, the potential to deteriorate the pollutant emissions, the thermal efficiency and the engine stability, increases and thus need to be carefully considered.

8. Although the *CNL* increased with boost pressure for a constant *RI*, the *CNLs* for all boost pressures and *RIs* collapsed onto a single curve when plotted against *PPRR*, indicating that *PPRR* is a more fundamental parameter for determining the *CNL*.

Regarding the effect of engine speed on the *CNL*:

9. The *CNL* substantially increases with engine speed (+ ~ 12 dB from 600 to 2400 RPM, for a given time-based *PPRR*). The increased magnitude of the “zero” mode in the ~ 400 to 2000 Hz range when engine speed is increased, results from a shift of the spectral power content from the combustion process to higher frequencies due to the increased cycle-repeat frequency.

10. The intensity of sound (*i.e.* the *CNL* expressed on a linear scale) does not increase in direct proportion to increases in engine speed. This would have been expected if the sound-intensity increase with speed was directly proportional to the number of combustion events per unit of time. Instead, the rate of the increase of the sound intensity with engine speed is much faster than expected from this simple approach. One explanation is that as the engine speed increases, the frequency components of the “zero” mode are shifted to higher frequencies that are less attenuated by the engine structure.

Finally, results from this study emphasize the fact that the *RI* and the *CNL* are designed to provide two distinctly different but complementary measurements. The *RI*, which correlates to the propensity of the combustion process to produce an acoustically resonating wave leading to knock, appears to be a better criterion for the sake of combustion investigations to avoid unwanted/knocking-combustion regimes. In contrast, the *CNL* provides a valuable indication of the overall loudness of the combustion event, regardless of whether or not a strong acoustic resonance (*i.e.* knock) is present.

## References

1. Dec, J.E. and Y. Yang, *Boosted HCCI for High Power without Engine Knock and with Ultra-Low NOx Emissions - using Conventional Gasoline.* SAE Int. J. Engines, 2010. **3**(1): p. 750-767. 10.4271/2010-01-1086.
2. Sellnau, M.C., et al., *Full-Time Gasoline Direct-Injection Compression Ignition (GDCI) for High Efficiency and Low NOx and PM.* SAE Int. J. Engines, 2012. **5**(2): p. 300-314. 10.4271/2012-01-0384.
3. Saxena, S. and I.D. Bedoya, *Fundamental phenomena affecting low temperature combustion and HCCI engines, high load limits and strategies for extending these limits.* Progress in Energy and Combustion Science, 2013. **39**(5): p. 457-488. http://dx.doi.org/10.1016/j.pecs.2013.05.002.
4. Yao, M., Z. Zheng, and H. Liu, *Progress and recent trends in homogeneous charge compression ignition (HCCI) engines.* Progress in Energy and Combustion Science, 2009. **35**(5): p. 398-437. 10.1016/j.pecs.2009.05.001.
5. Reitz, R.D., *Directions in internal combustion engine research.* Combustion and Flame, 2013. **160**(1): p. 1-8. 10.1016/j.combustflame.2012.11.002.
6. Dec, J.E., *Advanced compression-ignition engines—understanding the in-cylinder processes.* Proceedings of the Combustion Institute, 2009. **32**(2): p. 2727-2742. http://dx.doi.org/10.1016/j.proci.2008.08.008.
7. Xin, Q., *Overview of Diesel Engine Applications for Engine System Design - Part 1: Systems Engineering and Rational Considerations of Product R&D Organization Design.* 2011,SAE International, 10.4271/2011-01-2181.
8. Tsurushima, T., et al., *The Effect of Knock on Heat Loss in Homogeneous Charge Compression Ignition Engines.* 2002,SAE International, 10.4271/2002-01-0108.
9. Dec, J.E., Y. Yang, and N. Dronniou, *Improving Efficiency and Using E10 for Higher Loads in Boosted*

*HCCI Engines.* SAE Int. J. Engines, 2012. **5**(3): p. 1009-1032. 10.4271/2012-01-1107.

10. Dronniou, N. and J. Dec, *Investigating the Development of Thermal Stratification from the Near-Wall Regions to the Bulk-Gas in an HCCI Engine with Planar Imaging Thermometry.* SAE Int. J. Engines, 2012. **5**(3): p. 1046-1074. 10.4271/2012-01-1111.
11. Eng, J.A., *Characterization of Pressure Waves in HCCI Combustion.* 2002,SAE International, 10.4271/2002-01-2859.
12. Andreae, M.M., et al., *On HCCI Engine Knock.* 2007,SAE International, 10.4271/2007-01-1858.
13. Griffiths, J.F. and B.J. Whitaker, *Thermokinetic interactions leading to knock during homogeneous charge compression ignition.* Combustion and Flame, 2002. **131**(4): p. 386-399. http://dx.doi.org/10.1016/S0010-2180(02)00417-0.
14. Yelvington, P.E. and W.H. Green, *Prediction of the Knock Limit and Viable Operating Range for a Homogeneous-Charge Compression-Ignition (HCCI) Engine.* 2003,SAE International, 10.4271/2003-01-1092.
15. Dahl, D., M. Andersson, and I. Denbratt, *The Origin of Pressure Waves in High Load HCCI Combustion: A High-Speed Video Analysis.* Combustion Science and Technology, 2011. **183**(11): p. 1266-1281. 10.1080/00102202.2011.589875.
16. Vressner, A., et al., *Pressure Oscillations During Rapid HCCI Combustion.* 2003,SAE International, 10.4271/2003-01-3217.
17. Draper, C.S., *Pressure Waves Accompanying Detonation in the Internal Combustion Engine.* Journal of the Aeronautical Sciences (Institute of the Aeronautical Sciences), 1938. **5**(6): p. 219-226. 10.2514/8.590.
18. Shahlari, A.J., et al., *Comparison of Compression Ignition Engine Noise Metrics in Low-Temperature Combustion Regimes.* SAE Int. J. Engines, 2013. **6**(1): p. 541-552. 10.4271/2013-01-1659.
19. Vavra, J., et al., *Knock In Various Combustion Modes in a Gasoline-Fueled Automotive Engine.* Journal of Engineering for Gas Turbines and Power, 2012. **134**(8): p. 082807-082807. 10.1115/1.4006694.
20. Liu, Y., et al., *Experimental Study on the Characteristics of Knock under DI-HCCI Combustion Mode with Ethanol/Gasoline Mixed Fuel.* 2013,SAE International, 10.4271/2013-01-0544.
21. Szybist, J.P., et al., *Characterization of Engine Control Authority on HCCI Combustion as the High Load Limit is Approached.* SAE Int. J. Engines, 2013. **6**(1): p. 553-568. 10.4271/2013-01-1665.
22. Wissink, M., et al., *Investigation of Pressure Oscillation Modes and Audible Noise in RCCI, HCCI, and CDC.* 2013,SAE International, 10.4271/2013-01-1652.
23. Dec, J.E. and M. Sjöberg, *A Parametric Study of HCCI Combustion - the Sources of Emissions at Low Loads and the Effects of GDI Fuel Injection.* 2003,SAE International, 10.4271/2003-01-0752.
24. Sjöberg, M., J.E. Dec, and W. Hwang, *Thermodynamic and Chemical Effects of EGR and Its Constituents on HCCI Autoignition.* 2007,SAE International, 10.4271/2007-01-0207.
25. Sjöberg, M. and J.E. Dec, *Comparing late-cycle autoignition stability for single- and two-stage ignition fuels in HCCI engines.* Proceedings of the Combustion Institute, 2007. **31**(2): p. 2895-2902. http://dx.doi.org/10.1016/j.proci.2006.08.010.
26. Sjöberg, M. and J.E. Dec, *Influence of Fuel Autoignition Reactivity on the High-Load Limits of HCCI Engines.* SAE Int. J. Engines, 2008. **1**(1): p. 39-58. 10.4271/2008-01-0054.
27. Yang, Y., et al., *Tailoring HCCI heat-release rates with partial fuel stratification: Comparison of two-stage and single-stage-ignition fuels.* Proceedings of the Combustion Institute, 2011. **33**(2): p. 3047-3055. 10.1016/j.proci.2010.06.114.
28. Yang, Y., et al., *Partial Fuel Stratification to Control HCCI Heat Release Rates: Fuel Composition and Other Factors Affecting Pre-Ignition Reactions of Two-Stage Ignition Fuels.* SAE Int. J. Engines, 2011. **4**(1): p. 1903-1920. 10.4271/2011-01-1359.
29. Heywood, J.B., *Internal Combustion Engine Fundamentals*1988, New York: McGraw-Hill.
30. Johansson, T., et al., *HCCI Operating Range in a Turbo-charged Multi Cylinder Engine with VVT and Spray-Guided DI.* 2009,SAE International, 10.4271/2009-01-0494.
31. Dec, J.E., Y. Yang, and N. Dronniou, *Boosted HCCI - Controlling Pressure-Rise Rates for Performance Improvements using Partial Fuel Stratification with Conventional Gasoline.* SAE Int. J. Engines, 2011. **4**(1): p. 1169-1189. 10.4271/2011-01-0897.
32. Maria, A., et al., *Understanding Knock Metric for Controlled Auto-Ignition Engines.* 2013,SAE International, 10.4271/2013-01-1658.
33. Hyvönen, J., G. Haraldsson, and B. Johansson, *Operating Conditions Using Spark Assisted HCCI Combustion During Combustion Mode Transfer to SI in a Multi-Cylinder VCR-HCCI Engine.* 2005,SAE International, 10.4271/2005-01-0109.
34. Torregrosa, A.J., et al., *Combustion noise level assessment in direct injection Diesel engines by means of in-cylinder pressure components.* Measurement Science and Technology, 2007. **18**(7): p. 2131
35. Payri, F., et al., *Sound quality assessment of Diesel combustion noise using in-cylinder pressure components.* Measurement Science and Technology, 2009. **20**(1): p. 015107
36. Bhat, C.S., et al., *Influence of fuel injection parameters on combustion-induced noise in a small diesel engine.* International Journal of Engine Research, 2012. **13**(2): p. 130-146. 10.1177/1468087411428040.
37. Payri, F., et al., *New methodology for in-cylinder pressure analysis in direct injection diesel engines—application to combustion noise.* Measurement Science and Technology, 2005. **16**(2): p. 540
38. Sjöberg, M., et al., *Comparing Enhanced Natural Thermal Stratification Against Retarded Combustion Phasing for Smoothing of HCCI Heat-Release Rates.* 2004,SAE International, 10.4271/2004-01-2994.
39. Ji, C., et al., *Increasing the HCCI Autoignition Reactivity of Gasoline Using Conventional Ignition Improvers.* 8th U. S. National Combustion Meeting, 2013
40. Yang, Y., et al., *Boosted HCCI Combustion Using Low-Octane Gasoline with Fully Premixed and*

*Partially Stratified Charges.* SAE Int. J. Engines, 2012. **5**(3): p. 1075-1088. 10.4271/2012-01-1120.

## Contact Information

Corresponding authors: Jeremie Dernotte and John Dec, Sandia National Laboratories, MS-9053, P.O. Box 969, Livermore, CA 94551-0969, USA.

## Acknowledgments

The authors would like to thank Kenneth St. Hilaire, Christopher Carlen, David Cicone, Alberto Garcia and Gary Hubbard of Sandia National Laboratories for their dedicated support of the HCCI Engine Laboratory, Yi Yang (now at University of Melbourne, Australia) for collecting some of the data used in this analysis, Anthony Ruiz in regard to discussion about the frequency spectra, Wei Zeng and Magnus Sjoberg for valuable suggestions on the manuscript.

This work was performed at the Combustion Research Facility, Sandia National Laboratories, Livermore, CA, Support was provided by the U.S. Department of Energy, Office of Vehicle Technologies. Sandia is a multiprogram laboratory operated by the Sandia Corporation, a Lockheed Martin Company, for the United States Department of Energy's National Nuclear Security Administration under contract DE-AC04-94AL85000.

## Definitions/Abbreviations

### Greek Symbols

| | |
|---|---|
| $\alpha_{m,n}$ | Wave number in the wave Equation 4 |
| $\beta$ | Scale coefficient in the ringing intensity correlation (Equation 2) |
| $\Phi_m$ | Charge-mass equivalence ratio defined in the text |
| $\gamma$ | Ratio of specific heats = $c_p/c_v$ |
| $\rho$ | Density |
| $\theta$ | Refer to the crank angle |

### Std. symbols

| | |
|---|---|
| ***A/F*** | Air Fuel mass ratio of the fuel for complete combustion |
| **AHRR** | Apparent Heat Release Rate |
| ***B*** | Cylinder Bore |
| ***BDC*** | Bottom Dead Center |
| ***c*** | Speed of sound |
| **CA** | Crank Angle |
| ***CA50*** | Crank Angle of 50% burn point |
| ***CNL*** | Combustion Noise Level |
| ***CR*** | Compression Ratio |
| **EGR** | Exhaust Gas Recirculation |
| $(F/A)_{stoich}$ | Mass ratio of stoichiometric fuel/air mixture for complete combustion |
| ***F/C*** | Mass ratio of fuel and total inducted charge gas (*i.e.* fresh air and EGR) |
| **FFT** | Fast Fourier Transform |
| $f_{m,n}$ | Frequency of the vibration mode |
| **GDI** | Gasoline-type Direct Injector |
| **HCCI** | Homogeneous Charge Compression Ignition |
| **HRR** | Heat Release Rate |
| $I_{sound}$ | Intensity of Sound |
| $IMEP_g$ | Gross Indicated Mean Effective Pressure |
| ***KI*** | Knock Index |
| **LTC** | Low Temperature Combustion |
| ***LHV*** | Latent Heat of Vaporization |
| ***MON* (or *M*)** | Motor Octane Number |
| $P_{in}$ | Intake Pressure |
| $P_{max}$ | Maximum cycle pressure |
| ***PRR*** | Pressure Rise Rate |
| ***PPRR*** | Peak Pressure Rise Rate |
| **PSD** | Power Spectral Density |
| ***RI*** | Ringing Intensity |
| ***RON* (or *R*)** | Research Octane Number |
| **RPM** | Rotations Per Minute |
| **SI** | Spark Ignition |
| **SOI** | Start Of Injection |

| | |
|---|---|
| ***SP*** | Sound Pressure |
| $t$ | Period of the signal |
| **TDC** | Top Dead Center |
| $T_{in}$ | Intake Temperature |
| $T_{max}$ | Maximum mass-average cycle temperature |